Mitoquinone mesylate targets SARS-CoV-2 and associated lung inflammation through host pathways

Authors: Anton Petcherski[1, 10], Madhav Sharma[2, 10], Maria Daskou[2], Sandro Satta[2], Hariclea Vasilopoulos[2], Cristelle Hugo[2], Eleni Ritou[2], Barbara Jane Dillon[2], Eileen Fung[3], Gustavo Garcia Jr[4,5], Claudio Scafoglio[6], Arunima Purkayastha[7], Brigitte N Gomperts[8], Gregory A Fishbein[9], Vaithilingaraja Arumugaswami[4,5], Marc Liesa[1,4], Orian S Shirihai[1,4], Theodoros Kelesidis[2*]

Affiliations:

[1]Department of Medicine, Division of Endocrinology, David Geffen School of Medicine, University of California Los Angeles; Los Angeles, California, USA.

[2]Department of Medicine, Division of Infectious Diseases, David Geffen School of Medicine, University of California Los Angeles; Los Angeles, California, USA.

[3]Department of Surgery, David Geffen School of Medicine, University of California Los Angeles; Los Angeles, California, USA.

[4]Department of Molecular and Medical Pharmacology, David Geffen School of Medicine, University of California, Los Angeles; Los Angeles, California, USA.

[5]Eli and Edythe Broad Center of Regenerative Medicine and Stem Cell Research, University of California, Los Angeles; Los Angeles, California, USA.

[6]Department of Medicine, Division of Pulmonary and Critical Care Medicine, David Geffen School of Medicine, University of California Los Angeles; Los Angeles, California, USA.

[7]UCLA Children's Discovery and Innovation Institute, Mattel Children's Hospital UCLA, Department of Pediatrics, David Geffen School of Medicine, UCLA, Los Angeles, California, USA

[8]UCLA Children's Discovery and Innovation Institute, Mattel Children's Hospital UCLA, Department of Pediatrics, David Geffen School of Medicine, UCLA, Los Angeles, California, USA; Molecular Biology Institute, UCLA, Los Angeles, CA, USA; Jonsson Comprehensive Cancer Center, UCLA, Los Angeles, CA, USA; Eli and Edythe Broad Stem Cell Research Center, UCLA, Los Angeles, CA, USA; Division of Pulmonary and Critical Care Medicine, Department of Medicine, David Geffen School of Medicine, UCLA, Los Angeles, CA, USA.

[9]Department of Pathology, The David Geffen School of Medicine at UCLA, Los Angeles, California.

[10]These authors contributed equally to this work.

*Corresponding author. Email: tkelesidis@mednet.ucla.edu

Summary:

To date, there is no effective oral antiviral against SARS-CoV-2 that is also anti-inflammatory. Herein, we show that the mitochondrial antioxidant mitoquinone/mitoquinol mesylate (Mito-MES), a dietary supplement, has potent antiviral activity against SARS-CoV-2 and its variants of concern *in vitro* and *in vivo*. Mito-MES had nanomolar *in vitro* antiviral potency against the Beta and Delta SARS-CoV-2 variants as well as the murine hepatitis virus (MHV-A59). Mito-MES given in SARS-CoV-2 infected K18-hACE2 mice through oral gavage reduced viral titer by nearly 4 log units relative to the vehicle group. We found *in vitro* that the antiviral effect of Mito-MES is attributable to its hydrophobic dTPP+ moiety and its combined effects scavenging reactive oxygen species (ROS), activating Nrf2 and increasing the host defense proteins TOM70 and MX1. Mito-MES was efficacious reducing increase in cleaved caspase-3 and inflammation induced by SARS-CoV2 infection both in lung epithelial cells and a transgenic mouse model of COVID-19. Mito-MES reduced production of IL-6 by SARS-CoV-2 infected epithelial cells through its antioxidant properties (Nrf2 agonist, coenzyme Q_{10} moiety) and the dTPP moiety. Given established safety of Mito-MES in humans, our results suggest that Mito-MES may represent a rapidly applicable therapeutic strategy that can be added in the therapeutic arsenal against COVID-19. Its potential *long-term* use by humans as diet supplement could help control the SARS-CoV-2 pandemic, especially in the setting of rapidly emerging SARS-CoV-2 variants that may compromise vaccine efficacy.

One-Sentence Summary: Mitoquinone/mitoquinol mesylate has potent antiviral and anti-inflammatory activity in preclinical models of SARS-CoV-2 infection.

Keywords: Mitochondrial antioxidants, antiviral, SARS-CoV-2, inflammation, lung damage, COVID-19

Introduction:

The SARS-CoV-2 pandemic emphasizes the urgent need to determine cellular pathways that can be targeted by novel antivirals. Ideal antivirals would be given orally as soon as possible after disease onset and should not only limit replication of rapidly evolving SARS-CoV-2 variants but also associated inflammation that drives morbidity in COVID-19(Hu et al., 2021). The current treatments for COVID-19 have limitations. Remdesivir has shown limited therapeutic efficacy(Ansems et al., 2021). Dexamethasone might suppress host antiviral responses. Monoclonal antibodies are not oral, may not work against neutralization-resistant variants and may even increase inflammation(Lee et al., 2020). Current antivirals in development against SARS-CoV-2 such as nirmatrelvir/ritonavir and molnupiravir do not have anti-inflammatory effects. Molnupiravir may interfere with host RNA polymerases and may be mutagenic in cells(Zhou et al., 2021). Nirmatrelvir/ritonavir could cause severe or life-threatening interactions with widely used medications, including statins and blood thinners. Thus, there is a continued need for the development of oral safe antivirals for treatment of COVID-19.

Increased reactive oxygen species (ROS) contribute to the pathogenesis driven by respiratory syncytial virus (RSV)(Hu et al., 2019) and coronavirus(Shin et al., 2019). Mitochondria are a major source of ROS (mito-ROS). Aging compromises mitochondrial function and leads to increased production of mito-ROS(Braakhuis et al., 2018). Thus, decreasing mito-ROS and improving mitochondrial health may have broad health benefits including COVID-19 patients in

high-risk age groups. Mitoquinone and/or mitoquinol mesylate (Mito-MES) is the only mitochondrial antioxidant approved for human use which has been reported to support healthy aging (Braakhuis et al., 2018). It can safely be delivered orally long-term to humans and it has been used in clinical trials for ROS-related diseases (Rossman et al., 2018; Smith and Murphy, 2010). Mito-MES is coenzyme Q_{10} (CoQ_{10}) conjugated to a lipophilic cation (TPP)(Smith and Murphy, 2010). CoQ_{10} is the endogenous mitochondrial coenzyme involved in electron transfer and protection from lipid peroxidation (Smith and Murphy, 2010). Inside mitochondria, mitoquinone is being converted to its reduced active ubiquinol form, mitoquinol(Smith and Murphy, 2010). Given that Mito-MES is antiviral against RSV(Hu et al., 2019), which has similar mechanisms to evade host inflammatory responses to coronaviruses (Torres et al., 2015), we investigated whether Mito-MES is antiviral against SARS-CoV-2.

Results

Mito-MES decreases SARS-CoV-2 replication *in vitro*

We determined the effects of Mito-MES on SARS-CoV-2 replication first in Vero-E6 cells. We found that Mito-MES had a higher half maximal inhibitory concentration (IC50) against SARS-CoV-2 (Figure 1A), compared to remdesivir (RDV) (Figure 1B). The antiviral effect of 100-750 nM Mito-MES was confirmed by immunofluorescence (IF) detection of SARS-CoV-2 (Figure S1A) and by qPCR (Figure S1B). Given that intracellular levels of viral proteins is a better parameter determining coronavirus infection, we used flow cytometry to quantify the intracellular content of SARS-CoV-2 Spike S and the Nucleocapsid proteins (NP). Flow cytometry further confirmed that 1000 nM Mito-MES reduced cellular levels of SARS-CoV-2 N (Figure S1C) and S proteins (Figure S1D). There was no cytotoxicity induced by Mito-MES

across the effective dose range (10-1000 nM) in non-infected cells, based on XTT assay (Figure 1A).

Given that Vero-E6 cells lack interferon I (IFN-I), which regulates antiviral response against SARS-CoV-2(Hu et al., 2021), we tested Mito-MES in IFN-I competent human lung epithelial Calu-3 (Calu3) cells. Notably, the IC50 of Mito-MES against SARS-CoV-2 measured by TCID50 was 16-fold lower than remdesivir (Figure 1C and 1D). The antiviral efficacy of 10-1000 nM Mito-MES as assessed by IF (Figures 1E and S1E) and qPCR (Figure S1F) was much higher in Calu3 than in Vero-E6 cells. Flow cytometry further confirmed that Mito-MES attenuated the percent of SARS-CoV-2 infected Calu3 cells (Figure S1G and S1H). The anti–SARS-CoV-2 activity of Mito-MES was also confirmed in additional human cells including HEK 293T expressing ACE2 (Figure S1I) and human airway epithelial (HAE) cells in air-liquid interface (ALI) cultures (Figure 1F). We confirmed by flow cytometry the antiviral efficacy of Mito-MES in human FOXJ1 positive ciliated epithelial cells infected with SARS-CoV-2 (Figure S1J), as these ciliated epithelial cells are the main cells infected by SARS-CoV-2 in the lower respiratory tract (Hu et al., 2021). In summary, our results show that Mito-MES has potent antiviral activity against SARS-CoV-2 at the nM level in interferon competent human epithelial cells. Our data are consistent with data from Codo et al that showed that pretreatment with Mito-MES inhibited SARS-CoV-2 replication in monocytes (Codo et al., 2020). However, monocytes have little to no expression of ACE2 and it remains unclear whether monocytes and macrophages contribute to viral spread and COVID-19 disease progression (Hu et al., 2021). Herein, we provide the first evidence that Mito-MES directly attenuates SARS-CoV-2 replication in airway epithelial cells, the main target of SARS-CoV-2.

Mito-MES is antiviral against various coronaviruses

Given that Mito-MES targets host cellular targets that impact replication of coronaviruses, we hypothesized that Mito-MES has also antiviral activity against SARS-CoV-2 variants of concerns (VOCs) and other coronaviruses. Mito-MES inhibited *in vitro* SARS-CoV-2 B.1.351 (Beta) (IC50=0.034 μM) (Figure 2A) and B.1.617.2 (Delta) (IC50=0.041 μM) variants (Figure 2B) in Calu3 cells. Mito-MES 1000 nM also inhibited SARS-CoV-2 Delta variants in ALI lung cultures (Figure 2C). Mito-MES inhibited murine hepatitis virus (MHV-A59) in mouse 17Cl-1 fibroblasts (IC50=0.310 μM) (Figure 2D) as well as SARS-CoV-2 Delta variant in mouse lung cells from K18-hACE2 mice (IC50=1.6 μM) (Figure 2E) and was more potent antiviral than remdesivir (Figure 2F). Our data suggest that Mito-MES can be a useful antiviral therapy for coronaviruses, especially in the setting of rapidly emerging SARS-CoV-2 variants.

The TPP moiety of Mito-MES is antiviral

To elucidate the mechanism of action through which Mito-MES inhibits SARS-CoV-2, we compared the antiviral effects of Mito-MES administered before or concurrently with SARS-CoV-2. We found that 1000 nM Mito-MES inhibited NP expression in Calu3 cells when added before infection (effect on viral entry) but also when added 4 hours post infection (hpi), which allows time for viral entry, in both Calu3 (Figure 2G) and hACE2 HEK293T cells (Figure 2H) infected with Beta variant of SARS-CoV-2. These results suggest that Mito-MES inhibits both viral entry and cytoplasmic replication.

To gain further insight into the impact of Mito-MES on host cellular factors used by SARS-CoV-2 for entry in epithelial cells(Hu et al., 2021), we used flow cytometry to determine that Mito-MES did not impact the levels of ACE2, TMPRSS2, CD147 and NRP1 proteins in infected and uninfected Calu3 cells (Figure S2). Given that the hydrophobic TPP moiety of Mito-MES facilitates its entry through phospholipid bilayers (James et al., 2007) important for SARS-CoV-2 entry(Hu et al., 2021), we hypothesized that the TPP of Mito-MES per se is antiviral against SARS-CoV-2. We confirmed by viral titer assays in both hACE2 HEK293T cells and ALI HAE cultures that 1000 nM TPP was not cytotoxic but had potent antiviral activity against the Beta and Delta variants (Figure 2I and 2J), respectively. TPP reduced SARS-CoV-2 entry in hACE2 HEK293T cells but had less impact on SARS-CoV-2 cytoplasmic replication (Figure 2I). Collectively, these data showed that antiviral activity of Mito-MES in epithelial cells is partially mediated through its TPP moiety.

Interferon cellular pathways as mediators of the antiviral activity of Mito-MES

Given that Mito-MES was less antiviral in interferon deficient Vero-E6 cells compared to human cells (Figure 1), we hypothesized that its antiviral activity is mediated through interferon pathways. First, we assessed the impact of Mito-MES on key mitochondrial proteins that mediate interferon responses such as the mitochondrial antiviral signaling (MAVS) and the translocase of the outer membrane 70 (TOM70) (Liu et al., 2010; Sena and Chandel, 2012). Using flow cytometry, we found that Mito-MES had no impact on MAVS content (Figures S3A-S3C) but increased TOM70 protein (Figures S3D-S3F) in SARS-CoV-2 infected and uninfected Calu3 cells. These data were confirmed by immunofluorescence (Figures S3G and S3H). Next, we

assessed the impact of Mito-MES on extramitochondrial proteins that mediate interferon responses. The stimulator of interferon genes (STING)(Liu et al., 2010) together with mito-ROS participate in retinoic acid-inducible gene I (RIG-I)-like receptors signaling to regulate IFNs (Sena and Chandel, 2012). Mito-MES did not impact STING in SARS-CoV-2 infected Calu3 cells (Figures S4A-S4C). In Mito-MES treated compared to vehicle treated uninfected Calu3 cells, flow cytometry also demonstrated that Mito-MES increased levels of MX1 (Figures S4D-S4F), a key antiviral effector in COVID-19 patients(Bizzotto et al., 2020) that interacts with mitochondria(Cao et al., 2020). Lastly, using ELISA we found that at 48 hpi, Mito-MES did not impact increase in secreted IFN-β and IFN- λ in cell culture supernatants of SARS-CoV-2 infected Calu3 cells (Figures S4G and S4I). Mito-MES also did not impact cellular content of IFN-β and IFN- λ of SARS-CoV-2 infected Calu3 cells (Figure S4H and S4J). Overall, our data demonstrate that Mito-MES does not upregulate IFN-β, IFN-λ, MAVS and STING protein content in SARS-CoV-2 infected Calu3 cells, while it selectively induces mediators of IFN-I (TOM70 and MX1) which can explain better antiviral activity in interferon competent cells.

The antioxidant activity of Mito-MES partially mediates its antiviral activity

SARS-CoV2 infection increases mito-ROS(Codo et al., 2020). Given that antiviral activity of Mito-MES is still present in interferon deficient cells and that the antiviral activity of Mito-MES against RSV is mainly achieved by decreasing mito-ROS (Hu et al., 2019), we hypothesized that the antioxidant activity of Mito-MES is a major contributor to its anti-SARS-CoV-2 activity. In SARS-CoV-2 infected Calu3 cells, flow cytometry showed that Mito-MES reduced fluorescence of the mitochondrial superoxide reporter MitoSOX Red (Figure S5A-S5D). Consistent with the

importance of the TPP bringing Coenzyme Q10 (CoQ_{10}), inside mitochondria to scavenge ROS more efficiently, only higher concentrations (1000-2000 nM) of CoQ_{10}, had antiviral activity against both the Beta and the Delta strain in hACE2 HEK293T (Figure 2I) and HAE cells (Figure 2K). Both Mito-TEMPO, an independent mitochondrial antioxidant (Zielonka et al., 2017), and Mito-MES had potent and similar antiviral activity against SARS-CoV-2 in Calu3 cells (Figure 2L and 2M) and Vero-E6 cells (Figure S5E) at 1000 nM and as low as 25 nM.

Notably, consistent with prior evidence that very high concentrations of Mito-MES can have *in vitro* prooxidant effect that does not appear *in vivo* (Rodriguez-Cuenca et al., 2010), treatment with 1000 nM Mito-MES increased ROS levels in Calu3 cells, while preserving potent antiviral activity (Figure 2M). Consistent with prior data that excessive ROS scavenging decreases mitochondrial function, Mito-MES treatment at concentrations 50-1000 nM that displayed anti-SARS-CoV2 activity reduced mitochondrial oxygen consumption *in vitro* regardless of SARS-CoV-2 infection status (Figure S5F-S5I)(Fink et al., 2012). Consequently, mitochondrial respirometry further supported that mitochondrial scavenging of ROS or changes in mitochondrial respiration are not the main mediators of the anti-SARS-CoV-2 activity of Mito-MES in Calu3 cells.

Mito-MES is antiviral through the Nrf2 antioxidant pathway

In view of our data that the anti-SARS-CoV-2 activity of Mito-MES may be mediated through non-mitochondrial antioxidant pathways (Figure 2) and since Mito-MES induces the antiviral antioxidant Nrf2 pathway in epithelial cells(Zhang et al., 2020), we hypothesized that the antiviral activity of Mito-MES against SARS-CoV-2 in lung cells is mediated through the

Nrf2 pathway. To confirm our hypothesis, we pretreated Calu3 cells with the Nrf2 agonist Dimethyl fumarate (DMF) that is cytoprotective at lower concentrations (<25 μM)(Saidu et al., 2017). Pretreatment of Calu3 with 10 μM DMF for 24 hours increased anti–SARS-CoV-2 activity of 10-1000 nM Mito-MES as measured by flow cytometry (Figure 3A). The additive anti–SARS-CoV-2 activity of Mito-MES was decreased under a higher (100 μM) concentration of DMF known to be less cytoprotective (Figure 3A)(Saidu et al., 2017). Use of TCID50 assay confirmed these data (Figure 3B). The combination of Mito-MES with DMF also reduced the IC50 of Mito-MES by 3-fold (Figure 3C). Flow cytometry also showed that pretreatment with Mito-MES and DMF did not impact protein levels of Nrf2 (Figure S6) but reduced protein levels of the endogenous Nrf2 inhibitor, Keap1(Saha et al., 2020) (Figure S7) in infected and uninfected Calu3 cells. Pretreatment of Calu3 cells with 10 μM but not with 100 μM DMF, 100-1000 nM Mito-MES or the combination of Mito-MES with DMF, increased protein levels of heme oxygenase-1 (HO-1) (Figure S8), a key antiviral protein of the Nrf2 pathway(Saha et al., 2020). 100 μM DMF, but not 0.25 μM brusatol and 10 μM DMF, were cytotoxic in similarly treated uninfected cultures (Figure 3D).

Pretreatment of Calu3 for 24 hours with the Nrf2 small-molecule inhibitor brusatol (0.25 μM)(Saidu et al., 2017) significantly increased SARS-CoV2 replication as assessed by TCID50(Figure 3E) and flow cytometry (Figure 3F) and inhibited the antiviral effect of Mito-MES. Pretreatment with brusatol reduced protein levels of Nrf2 (Figure S6) and increased protein levels of Keap (Figure S7) in infected and uninfected Calu3 cells. Pretreatment of Calu3 with 0.25 μM brusatol did not have an impact on the effect of Mito-MES on HO-1 protein levels (Figure S8). Collectively, our data suggest that the antiviral activity of Mito-MES against SARS-

CoV-2 is partially mediated through the Nrf2 pathway which may not be reflected by the total cellular protein levels of Nrf2 and Keap and is not mediated by the HO-1 protein.

Nrf2 pathway also regulates apoptosis of lung cells (Saha et al., 2020) which is associated with viral replication, lung injury and severe COVID-19(Hu et al., 2021). Thus, we assessed the impact of Mito-MES on cellular apoptosis associated with SARS-CoV-2 infection. Immunostaining showed that Mito-MES reduced SARS-CoV-2-induced increase in cleaved caspase 3, a key regulator of apoptosis in both Vero-E6 (Figures S9A-S9E) and Calu3 cells (Figure S9F).

Our data are in agreement with Olagnier et al who showed that the Nrf2 agonist DMF had anti-SARS-CoV2 activity which is not mediated through HO-1(Olagnier et al., 2020). Of note a much higher cytotoxic (Saidu et al., 2017) concentration of DMF (200 μM) was used in their study.

Mito-MES shows anti-SARS-CoV-2 efficacy in mice *in vivo*

The anti-SARS-CoV-2 activity of Mito-MES at the nM level can be achieved therapeutically *in vivo* with oral Mito-MES that has good bioavailability at the respiratory mucosa(Smith and Murphy, 2010). Accordingly, doses of Mito-MES in mice of 4 mg/kg/day achieve good lung tissue penetration and have been translated to oral doses in humans(Smith and Murphy, 2010). Therefore, we tested the *in vivo* efficacy of Mito-MES to reduce viral replication in the lung of K18-hACE2 mice infected with SARS-CoV-2 (Figure 4)(White et al., 2021). As a proof-of-principle *in vivo* experiment and to ensure adequate Mito-MES levels in the murine lung tissue at the time of SARS-CoV-2 infection, we performed prophylactic dosing of 4 mg/kg Mito-MES

intraperitoneally (i.p) 24 hours before SARS-CoV-2 infection that was continued daily for 3 days following infection (Figure 4A). There was a reduction of nearly 3 log units in SARS-CoV-2 viral titers in the lungs of the Mito-MES group relative to the vehicle control group (Figures 4B and 4C), which is higher than the anti-SARS-CoV-2 effect of remdesivir in K18-hACE2 mice (White et al., 2021). The anti-SARS-CoV-2 activity of Mito-MES was also seen in mice that were treated with 4 mg/kg Mito-MES 8 hpi (Figures 4B and 4C). We then assessed whether oral Mito-MES derived from the formulation given to humans as a dietary supplement capsule is antiviral against the Delta variant *in vivo* (Figure 4D). Mito-MES treatment in SARS-CoV-2 infected K18-hACE2 mice through oral gavage at concentration 20 mg/kg/day reduced viral titer by nearly 4 log units relative to the vehicle group (Figure 4E). The anti-SARS-CoV-2 activity of Mito-MES was confirmed by ELISA that showed that SARS-CoV-2 NP levels were reduced in lungs of infected K18-hACE2 mice that were treated with Mito-MES versus vehicle (Figure 4F). Given that Mito-MES acts in both epithelial and endothelial cells(Smith and Murphy, 2010) and to fully characterize the anti–SARS-CoV-2 activity at the single cell level, we determined by flow cytometry levels of SARS-CoV-2 NP among lung cell subtypes in murine lung (see gating strategy in Figure S10) after 3 days post infection (dpi), when viral replication is the highest (Winkler et al., 2020). We confirmed that Mito-MES had anti–SARS-CoV-2 activity among lung epithelial cells (Figures 4G-4I, S11A and S11B) that was high in ciliated lung epithelial cells (Figures 4 J-L; Figures S11C and S11D). Mito-MES had antiviral activity in alveolar type 1 (AT1) (Figure S12A-S12D), AT2 (Figure S12E-S12H) cells, endothelial cells (Figure S12I-S12L). Taken together, these experiments show that Mito-MES treatment can reduce the replication of SARS-CoV-2 by at least 3 orders of magnitude in mouse model of SARS-CoV-2 infection. Given that Mito-MES works through host mechanisms and has higher antiviral activity

against coronaviruses in human compared to mouse cells (Figure 2), Mito-MES has compelling potential for clinical efficacy for the treatment of COVID-19.

Mito-MES is anti-inflammatory in SARS-CoV-2 infection

Increased release of IL-1β and IL-6 by SARS-CoV-2 infected epithelial cells is associated with lung injury and severe COVID-19(Hu et al., 2021). Given previously described anti-inflammatory effects of Mito-MES(Smith and Murphy, 2010), we also assessed the impact of Mito-MES on SARS-CoV-2-associated inflammatory responses. Using ELISA and Luminex immunoassays, we found that Mito-MES attenuated SARS-CoV-2-induced increase in secretion of IL-6 by Calu3 (Figures 5A and 5B) cells and of IL-6 and IL-1β in upper (Figure 5C) and lower (Figure 5D) airway respiratory epithelium ALI cultures. Our data is consistent with prior evidence that Mito-MES attenuates ROS, activation of inflammasome, NFκB signaling that collectively drive a cytokine storm, release of IL-1β, IL-6 (Zhang et al., 2020) and ultimately lung damage in viral infections (Hu et al., 2019). In conclusion, our results show that Mito-MES not only has antiviral activity against SARS-CoV-2 but also attenuates inflammatory responses of the infected epithelial cells that drive severe lung injury in COVID-19.

Mito-MES is anti-inflammatory in SARS-CoV-2 infection through its antioxidant properties and the TPP moiety.

Since Mito-MES is anti-inflammatory(Smith and Murphy, 2010) and an agonist of Nrf2 that has a major role in regulation of inflammation and reduces production of IL-1β and IL-6 (Saha et

al., 2020), we hypothesized that not only the antiviral but also the anti-inflammatory activity of Mito-MES in SARS-CoV-2 infection is mediated through the Nrf2 pathway. Pretreatment of Calu3 cultures with 10 μM of the Nrf2 agonist DMF for 24 hours resulted in reduction in subsequent release of IL-6 to the cell supernatant from infected cells at 48 hpi as measured by immunoassays (Figure 5E). Compared to treatment of Calu3 with 1000 nM Mito-MES alone, treatment of Calu3 with 10 or 100 μM DMF in combination with Mito-MES for 72 hours resulted in an additive reduction in release of IL-6 to the cell supernatant from SARS-CoV-2 infected cells (Figure 5E). Pretreatment of Calu3 with 0.25 μM of the Nrf2 inhibitor brusatol (Saidu et al., 2017) significantly increased subsequent release of IL-6 by infected cells (Figure 5F) and inhibited the anti-inflammatory effect of Mito-MES (Figure 5F). Notably, the dTPP moiety and the mitochondrial antioxidant CoQ_{10} also reduced subsequent release of IL-6 to the cell supernatant from SARS-CoV-2 infected ALI cultures (Figure 5G). Collectively, these data suggest that Mito-MES reduces production of IL-6 by SARS-CoV-2 infected epithelial cells through its antioxidant properties (Nrf2 agonist, CoQ_{10} moiety, antioxidant against mito-ROS) and the dTPP moiety.

Mito-MES shows *in vivo* anti-inflammatory efficacy in mouse model of SARS-CoV-2 infection

We then tested the *in vivo* anti-inflammatory efficacy of 4 mg/kg intraperitoneal daily dosage of Mito-MES in K18-hACE2 mice infected with the SARS-CoV-2 wild type (WT)(cohort A) as early as 3 dpi and in K18-hACE2 mice infected with Beta variant (cohort B), after 5-7 dpi, when lung inflammation is the highest (Winkler et al., 2020)(Figure 6A). Using Luminex

immunoassays we showed that there was a reduction of at least 2 orders of magnitude in IL-1β (Figure 6B) and IL-6 (Figure 6C) in the lungs of the Mito-MES treated SARS-CoV-2 infected relative to the vehicle treated group as early as 3 dpi. The Mito-MES-induced reduction in IL-1β and IL-6 in the lung after 5-7 dpi was confirmed in mice from cohort B infected with the SARS-CoV-2 Beta variant (Figures 6D and 6E). Mito-MES did not change protein levels of IL-18 (Figures S13A and S13C) and did not consistently reduce levels of TNF-α in SARS-CoV-2 infected K18-hACE2 mice (Figure S13B and S13D). To fully characterize the anti–inflammatory activity of Mito-MES at the cell level, we determined the infiltration of different immune cell subtypes into murine lungs by flow cytometry (see gating strategy in Figure S14). Mito-MES reduced frequency of CD45+ immune as early as 3 dpi in mice infected with WT SARS-CoV-2 (Figures 6F and 6G) but not at 5 dpi in mice infected with the Beta variant SARS-CoV-2 (Figure S13E). Mito-MES also reduced frequency of NK cells in murine lungs of mice infected with both the WT and the Beta variant SARS-CoV-2 (Figures S15M-S15O). Mito-MES did not alter frequency of neutrophils (Figure S15A-S15C), macrophages (Figure S15D-S15F), myeloid dendritic cells (DCs) (Figure S15G-S15I), lymphoid DCs (Figure S15J-S15L), T cells (Figure S15P-S15R) and B cells (Figures S15S and S15T). Immunofluorescence analysis showed that Mito-MES inhibited SARS-CoV-2-associated increase in cleaved caspase 3, a marker of tissue apoptosis and damage, in K18-hACE2 mice infected with Beta variant (Figure S13F). Histopathology analysis also showed a reduction of lung inflammation and tissue damage in Mito-MES treated mice over vehicle-treated mice at day 5-7 after infection (Figures 6H to 6J). Taken together, these experiments show that Mito-MES treatment has an anti-inflammatory effect that is seen at both early and late stages of SARS-CoV-2 infection and has good therapeutic efficacy against COVID-19 *in vivo*.

Discussion

The SARS-CoV-2 pandemic necessitates the development of antiviral and anti-inflammatory therapeutics that can be rapidly moved into the clinic. Herein, we demonstrate that Mito-MES has *in vitro* and *in vivo* antiviral, antiapoptotic and anti-inflammatory effects on SARS-CoV-2 infected epithelial cells. Unlike vaccines, attenuation of detrimental host responses that propagate viral replication may be efficacious even in the setting of mutant strains of SARS-CoV-2 to which viral-targeted therapeutics and vaccines may be less effective. Mito-MES had nanomolar antiviral potency against the Beta and Delta SARS-CoV-2 variants as well as MHV. Thus, Mito-MES is expected to have antiviral activity against rapidly emerging SARS-CoV-2 variants such as the B.1.1.159 (omicron) variant.

We show that the antiviral effect of Mito-MES against SARS-CoV-2 in epithelial cells is mediated partially through its antioxidant properties (reduces mito-ROS and induces the Nrf2 pathway) and through the hydrophobic dTPP cation that integrates into cellular membranes that are important for SARS-CoV-2 replication(Hu et al., 2021). Mito-MES had more potent antiviral activity in interferon competent epithelial cells compared to interferon deficient Vero-E6 cells and it induced mitochondrial mediators of IFN-I responses (TOM70 and MX1) that have an important role in host cellular responses against SARS-CoV-2 (Bizzotto et al., 2020). The anti-inflammatory effect of Mito-MES was mostly seen against IL-6 and NK cell infiltration in SARS-CoV-2 infected mouse lungs. Importantly, Mito-MES at nanomolar concentrations had additive antiviral and anti-inflammatory activity together with DMF which is currently used as an anti-inflammatory drug in relapsing-remitting multiple sclerosis(Blair, 2019). Thus, the

combination of an FDA-approved drug (DMF) with Mito-MES could easily be repurposed and tested in clinical trials to establish a potent novel combined antiviral *and* anti-inflammatory therapeutic strategy in COVID-19 patients. Our data suggest that Mito-MES may have multiple favorable therapeutic effects in COVID-19 (Figure S16).

Although host-targeted antivirals may be toxic, the safety profile of Mito-MES is well established in humans. Mito-MES is currently available as a dietary supplement (10 mg orally daily) and its safety for up to one year in doses as high as 80 mg orally daily has been validated in independent clinical trials for oxidative damage-related diseases such as Parkinson's, hepatitis C, as well as vascular dysfunction (Rossman et al., 2018; Smith and Murphy, 2010). Thus, Mito-MES could easily be repurposed and tested in clinical trials as a small molecule inhibitor of SARS-CoV-2 replication and inflammation-induced pathology for outpatient treatment of mild to moderate acute COVID-19 and for post-exposure prophylaxis against SARS-CoV-2 in high-risk exposures.

To date, there is no safe, efficacious oral antiviral that is effective against SARS-CoV-2 variants, has anti-inflammatory activity and can *also* be given *long term* in humans. Both Mito-MES and CoQ_{10} are nutraceuticals that can be very useful as preexposure prophylaxis in high risk (un)vaccinated or immunocompromised patients where the SARS-CoV-2 vaccines may have low efficacy. The favorable antiviral, antioxidant and anti-inflammatory properties of Mito-MES, its use for treatment of neurodegenerative and heart diseases and its excellent safety profile in humans(Rossman et al., 2018; Smith and Murphy, 2010), can establish Mito-MES as a novel therapeutic strategy for Post-acute COVID-19 syndrome (PACS) where residual low-grade SARS-CoV-2 replication in combination with aberrant proinflammatory mechanisms have been observed (Nalbandian et al., 2021). Finally, Mito-MES can have a favorable effect on

comorbidities associated with morbidity in COVID-19 such as vascular dysfunction and aging(Rossman et al., 2018; Smith and Murphy, 2010). To date, an oral therapy for COVID-19 and PACS that has anti-inflammatory, antiviral, antiapoptotic properties and favorable impact on comorbidities such as vascular dysfunction, does not exist. Mito-MES may represent a rapidly applicable therapeutic strategy that can be added in the therapeutic arsenal against COVID-19.

Author contributions:

Conceptualization: TK

Methodology: AP, MS, MD, SS, HV, CH, ER, BJD, EF, GG, STR, CS, AP, BNG, GAF, VA, ML, OSH, TK

Investigation: AP, MS, MD, SS, HV, CH, ER, BJD, EF, GG, STR, CS, AP, BNG, GAF, VA, ML, OSH, TK

Visualization: AP, SS, TK

Funding acquisition: TK

Project administration: TK

Supervision: TK, OSH

Writing – original draft: AP, MS, TK

Writing – review & editing: AP, MS, SS, ML, OSH, TK

Acknowledgments:

The flow cytometry machine used in the study was purchased through the UCLA Center for AIDS Research (P30AI28697) grant. We thank Dani Dagan for helpful discussions and advice.

Funding: This work was supported in part by

National Institute of Health grant R01AG059501 (TK)

National Institute of Health grant R01AG059502 04S1 (TK)

California HIV/AIDS Research Program grant OS17-LA-002 (TK)

Declaration of interest

Competing interests: This manuscript is related to patents PCT/US2021/040869, US. Application No 63/166,207. Authors declare that they have no competing interests.

FIGURE LEGENDS

Figure 1. Mitoquinone mesylate strongly inhibits SARS-CoV-2 replication in multiple types of epithelial cells. (**A-D**) Vero-E6 cells [(**A**) and (**B**)], Calu3 cells [(**C**), (**D**)] were treated with indicated doses of remdesivir (RDV) [(**B**)(**D**)] or mitoquinone mesylate (Mito-MES) [(**A**), (**C**)]. IC50, 50% cytotoxic concentration (CC50) values are indicated. Viral replication at 48 hours post infection (hpi) by TCID50-assay. Cell cytotoxicity was assessed in uninfected cells at 48 hours by the XTT assay. **(E)** Immunofluorescent analysis (48 hpi) of infected Calu3 cells treated with Mito-MES (10 nM). Scale bar=50µm. **(F)** Viral replication by flow cytometry in human airway epithelial cells. For all experiments cells were infected with SARS-CoV-2 at an MOI of 0.1 and were treated with drugs for at least 2 hours before infection and throughout the experiment unless stated otherwise. For "Entry" treatment, the drugs were added to the cells for 2 h before infection and at 2 hpi and the virus–drug supernatant was then replaced with culture medium. In all panels, data are means ± SEM of at least three independent experiments with at least 3 replicates in each experiment.

Figure 2. Mitoquinone mesylate (Mito-MES) has antiviral activity against coronaviruses that partially depends on its lipophilic and antioxidant components. (**A-F**) Calu3, human airway epithelial (HAE) cells, 17CL-1 cells and lung cells isolated from K18-hACE2 mice were infected with SARS-CoV-2 Beta or Delta variant or mouse hepatitis virus (MHV) and treated with vehicle control (Ctrl) or Mito-MES versus remdesivir (RDV) as shown. Viral replication by TCID50-assay and XTT assay at 48 hpi. IC50, 50% cytotoxic concentration (CC50) values are indicated. (**G** to **I**) Time-of-addition experiment of RDV, Mito-MES, dTPP and coenzyme Q10

(CoQ_{10}) in Calu3 cells, hACE2 HEK293T cells [at entry, post-viral entry and throughout 24 hpi (full time)]. Levels of intracellular SARS-CoV-2 Nucleocapsid protein were determined by ELISA. [(**J**)(**K**)] Viral replication at 48 hpi by TCID50-assay in HAE cells treated with dTPP or CoQ_{10} as shown. [(**L**)(**M**)] Calu3 cells were treated as shown with Ctrl, Mito-TEMPO (MT) or Mito-MES and were infected with green fluorescent icSARS-CoV-2-mNG (MOI 0.3). Oxidative stress by dihydroethidum (DHE) fluorescence and viral replication at 48 hpi by SARS-CoV-2-mNG fluorescence and TCID50-assay (**L**) in Calu3 cells. For all experiments cells were infected with SARS-CoV-2 and treated as in Figure 1. In all panels, data are representative or mean ± SEM of at least two experiments in 3 replicates. Unless otherwise stated, statistical comparison was done between the Ctrl and each shown experimental group by using two-tailed Mann–Whitney (***$p < 0.001$).

Figure 3. The antiviral activity of Mito-MES against SARS-CoV-2 in epithelial cells is mediated through the Nrf2 pathway. (A-F) Calu3 cells infected with SARS-CoV-2 (48 h) (MOI 0.1) and treated with Mito-MES (10-1000 nM, 72 h) and/or the Nrf2 agonist Dimethyl fumarate (DMF) (10, 100 μM, 16-24 hrs) and/or the Nrf2 inhibitor brusatol (0.25 μM, 16-24 hrs) or DMSO vehicle control (Ctrl). (**A** to **C**) Viral replication by flow cytometry (**A**) or TCID50-assay at 48 hrs post infection (hpi) [(**B**), (**C**)] in Calu3 cells treated as shown. IC50 values for Mito-MES ± DMF 10 μM are shown (**C**). (**D**) Cell cytotoxicity (XTT assay) in uninfected Calu3 cells treated as shown for 24 hrs. [(**E**), (**F**)] Viral replication by TCID50-assay (**E**) or flow cytometry (**F**) at 48 hpi in Calu3 cells treated as shown. [(**G**)(**H**)] Protein levels of cleaved caspase-3 in Calu3 cells as assessed by immunofluorescence (**G**) or flow cytometry (**H**). Summary (means ± SEM) or representative data of at least three experiments in duplicates and

triplicates are shown. Each data-point represents one biological sample. Unless otherwise stated, statistical comparison was done between the Ctrl and each shown experimental group by using two-tailed Mann–Whitney (*$p < 0.05$, **$p < 0.01$, ***$p < 0.001$).

Figure 4. Mitoquinone mesylate (Mito-MES) inhibits SARS-CoV-2 replication in mouse model of SARS-CoV-2 infection. (**A**-**L**) hACE2 K18 mice were infected intranasally with SARS-CoV-2 (10,000 PFU/mouse) and lung tissue was harvested 72 hours post infection (hpi). Supernatants from lung homogenates were used for viral titer [based on cytopathic effect; CPE or measurement of intracellular SARS-CoV-2 nucleocapsid protein (NP) by ELISA] in Vero-E6 cells [(**B**), (**C**), (**E**)]. (**A**) Study design for cohort A. Mice were infected with wild type (WT) SARS-CoV-2 and treated with vehicle control (saline 10% DMSO; Ctrl) (n=5) or Mito-MES 4 mg/kg/day (n=10) given intraperitoneally 24 hours before the infection (hbi) (n=5) or 8 hpi (n=5). (**D**) Study design for cohort B. Mice were infected with SARS-CoV-2 Delta variant and treated through gavage with Ctrl (n=10) or Mito-MES 20 mg/kg/day (n=10) 24 hbi. (**F**) Measurement of SARS-CoV-2 NP by ELISA in lung homogenates. (**G** to **L**) Assessment of SARS-CoV-2 NP in EPCAM (+) lung cells (**G** to **I**) and FOXJ1(+) ciliated cells (**J** to **L**) by flow cytometry. Representative or summary (mean ± SEM) data from experiments in triplicates. Each data-point represents one biological sample. Unless otherwise stated, statistical comparison was done between the Ctrl and each shown experimental group by using two-tailed Mann–Whitney ***p<0.001, **p<0.01, *p<0.05.

Figure 5. Mitoquinone mesylate (Mito-MES) has anti-inflammatory activity in SARS-CoV-2 infected epithelial cells. [(**A**), (**B**)] Calu3 cells treated with vehicle control (Ctrl) or Mito-MES

(100 or 1000 nM, 72 hrs) and infected with wild type (WT) SARS-CoV-2 (48 hrs)(MOI 0.1). IL-6 was measured by ELISA (**A**) and other cytokines by Luminex immunoassay (**B**) in cell culture supernatants collected 48 hours post infection (hpi). (**C**) Large airway epithelial cells cultured in air-liquid interface (ALI) were treated with Ctrl or Mito-MES (1000 nM) and were infected with SARS-CoV-2 Delta variant (MOI 1). Cytokines were measured by Luminex immunoassay at 48 hpi. (**D**) As in (**C**) but a small distal airway epithelial ALI culture system was used. [**(E)**, **(F)**] Calu3 cells treated with Mito-MES (10-1000 nM, 72 hrs) and/or the Nrf2 agonist Dimethyl fumarate (DMF)(10, 100 μM, 16-24 hrs) (**E**) and/or the Nrf2 inhibitor brusatol (0.25 μM, 16-24 hrs)(**F**) and infected with WT SARS-CoV-2 (48 h)(MOI 0.1). Cytokines were measured by Luminex immunoassay at 48 hpi. (**G**) As in (**D**) but cells were treated with Mito-MES, dTPP and CoQ_{10} as shown. Data are pooled data (mean ± SEM) from three experiments in triplicates. Each data-point represents one biological sample. Unless otherwise stated, statistical comparison was done between the Ctrl and each shown experimental group by using two-tailed Mann–Whitney (*$p < 0.05$, **$p < 0.01$).

Figure 6. Mitoquinone mesylate (Mito-MES) inhibits SARS-CoV-2 associated inflammation and lung damage in mouse model of SARS-CoV-2 infection. hACE2 K18 mice were infected intranasally with SARS-CoV-2 wild type (WT) or Beta variant (10,000 PFU/mouse), treated with Mito-MES 4 mg/kg/day or vehicle control (Ctrl) and lung was harvested on day 3 (cohort A see Figure 4) or 5-7 (cohort B) post infection. (**A**) Study design of cohort B. (**B** to **E**) Supernatants from lung homogenates of mice from cohort A [(**B**), (**C**)] or B [(**D**), (**E**)] were used for measurement of cytokines using Luminex immunoassay. [(**F**), (**G**)] Flow cytometry assessed frequency of CD45+ immune cells in lungs from mice in cohort A.

Representative (**F**) and summary data (**G**). (**H-J**) Harvested lungs from mice in cohort B were paraffin-embedded and 5-µm sections were stained for hematoxylin and eosin. Histopathology score was determined according to Methods. Representative images of lung sections. Regions of the lung where inflammation was assessed are highlighted by red boxes and arrows. Normal regions of the lung are highlighted by yellow boxes. Representative or summary (mean ± SEM) data from experiments in triplicates. Each data-point represents one biological sample. Unless otherwise stated, statistical comparison was done between the Ctrl and each shown experimental group by using two-tailed Mann–Whitney ***$p<0.001$, **$p<0.01$, *$p<0.05$.

SUPPLEMENTAL FIGURE TITLES AND LEGENDS

Figure S1 (related to Figure 1). Mitoquinone mesylate (Mito-MES) inhibits SARS-CoV-2 replication in independent epithelial cell types. (**A** to **J**) Vero E6 [(**A**), (**B**), (**C**), (**D**)], Calu3 [(**E**), (**F**), (**G**), (**H**)] HEK293T-hACE2 (**I**) and human airway ciliated (positive for FOXJ1 protein) epithelial (**J**) cells were treated with 10 μM of remdesivir (RDV) [(**B**), (**F**)] or indicated doses of Mito-MES or DMSO vehicle control (Ctrl). Viral replication at 48 hrs post infection (hpi) by immunofluorescence [(**A**), (**E**)], qPCR [(**B**), (**F**)] or flow cytometry [(**C**), (**D**), (**G**), (**H**), (**I**), (**J**)]. Viral replication at the protein level was measured by assessing SARS-CoV-2 Spike (S) protein [(**A**), (**D**), (**E**), (**H**)] and nucleocapsid (**N**) protein [(**C**), (**G**), (**I**), (**J**)]. For all experiments cells were infected with SARS-CoV-2 at an MOI of 0.1 and they were treated with drugs for 2 hrs before infection and throughout the experiment until 48 hpi. In all panels summary data are presented as mean ± SEM or representative images of three or more experiments (with at least 2 replicates). Each data-point represents one biological sample. Unless otherwise stated, statistical comparison was done between the Ctrl and each shown experimental group by using two-tailed Mann–Whitney (*$p < 0.05$, **$p < 0.01$, ***$p < 0.001$).

Figure S2 (related to Figure 2). Impact of Mito-MES on host membrane proteins important for SARS-CoV-2 entry. (**A** to **L**) Assessment of levels of membrane proteins important for SARS-CoV-2 entry by flow cytometry in SARS-CoV-2 (un)infected Calu3 cells treated with Mito-MES (1000 nM, blue line) or vehicle control (Ctrl, red line) (72 h) and infected with SARS-CoV-2 (48 h). The negative stain control (fluorescence minus one; FMO) is shown in

light grey. (**A**) Median fluorescence intensity (MFI) of ACE2 in total Calu3 cells. (**B**) MFI of ACE2 in SARS-CoV-2 infected Calu3 cells. (**C**) % of total Calu3 cells positive for ACE2. (**D**) MFI of TMPRSS2 in total Calu3 cells. (**E**) MFI of TMPRSS2 in SARS-CoV-2 infected Calu3 cells. (**F**) % of total Calu3 cells positive for TMPRSS2. (**G**) MFI of Neuropilin 1 (NRP-1) in total Calu3 cells. (**H**) MFI of NRP-1 in SARS-CoV-2 infected Calu3 cells. (**I**) % of total Calu3 cells positive for NRP-1. (**J**) MFI of CD147 in total Calu3 cells. (**K**) MFI of CD147 in SARS-CoV-2 infected Calu3 cells. (**L**) % of total Calu3 cells positive for CD147. Representative data from at least three independent experiments with at least 2 replicates are shown.

Figure S3 (related to Figure 2). Impact of Mito-MES on mitochondrial proteins that mediate interferon host immune responses in SARS-CoV-2 infected epithelial cells. (**A** to **C**) Assessment of protein levels (fluorescence intensity and % of cells positive for the target protein) of MAVS by flow cytometry in total [(**A**), (**C**)] and SARS-CoV-2 infected (**B**) (48 hrs) Calu3 cells treated with Mito-MES (1000 nM, blue line) or vehicle control (Ctrl, red line) (72 hrs). [(**D**), (**E**), (**F**)] Assessment of protein levels of TOM70 by flow cytometry in total [(**D**), (**F**)] and SARS-CoV-2 infected (**E**) Calu3 cells [(**G**), (**H**)] Immunofluorescence shows levels of TOM70 in Calu3 cells at 48 hrs post-infection. (**G**) Representative panels show immunostaining for SARS-CoV-2 spike protein (green) and TOM70 (red) in uninfected cells, infected cells treated with Ctrl or Mito-MES (100 nM). DAPI stained cell nuclei. Scale bar= 100 μm. (**H**) Summary analysis of immunofluorescence experiments for TOM70 protein [median fluorescence intensity (MFI), arbitrary units]. Data in (**A** to **G**) are representative for three or more experiments with at least 2 replicates. Pooled data from at least three experiments in (**H**). Bars indicate mean ± SEM.

Statistical comparison was done between the Ctrl and each shown experimental group by using two-tailed Mann–Whitney (*$p < 0.05$, **$p < 0.01$, ***$p < 0.001$).

Figure S4 (related to Figure 2). Impact of Mito-MES on interferon host immune responses in SARS-CoV-2 infected epithelial cells. (**A** to **C**) Protein levels (fluorescence intensity and % of cells positive for the target protein) of STING were assessed by flow cytometry in total [(**A**), (**C**)] and SARS-CoV-2 infected (**B**) Calu3 cells. (**D** to **F**) Similarly, protein levels of MX1 were assessed by flow cytometry in total [(**D**), (**F**)] and SARS-CoV-2 infected (**E**) Calu3 cells. (**G** to **J**) ELISA was done to assess protein levels of secreted [(**G**), (**I**)] and cellular [(**H**), (**J**)] interferons [beta: IFN-β (**G**), (**H**), lambda: IFN-λ (**I**), (**J**)] in Calu3 cells treated with Mito-MES (100-1000 nM) or vehicle control (Ctrl) (72 h) and infected with SARS-CoV-2 (48 h). Data in (**A** to **F**) show representative data from at least three independent experiments. Data in (**G** to **J**) are pooled from three or more independent experiments with at least 2 replicates. Bars indicate mean ± SEM. Each datapoint represents one biological sample. Unless otherwise stated, statistical comparison was done between the Ctrl and each shown experimental group by using two-tailed Mann–Whitney.

Figure S5 (related to Figure 2). The antiviral activity of Mito-MES against SARS-CoV-2 in epithelial cells depends partially on its antioxidant activity. (**A** to **D**) Assessment of fluorescence [fluorescence intensity (MFI) (**A**), (**B**) and percent of positive cells (**C**), (**D**)] of MitoSOX Red in Calu3 cells infected with SARS-CoV-2 (48 hrs) and treated with Mito-MES (100 nM) or DMSO vehicle control (Ctrl). (**E**) Vero-E6 cells were treated with Ctrl, Mito-

TEMPO (MT) or Mito-MES and were infected with fluorescent SARS-CoV-2 (MOI 0.3) (48 hrs). Immunofluorescent analysis of viral replication and cellular oxidative stress [fluorescence of dihydroethidium (DHE)] at 48 hpi. (**F** to **H**) Seahorse XF Analyzer determined cellular bioenergetics [oxygen consumption rate (OCR) (**F**) and extracellular acidification rate (ECAR) (**G** to **I**) in live (un)infected Calu3 cells treated with Mito-MES or Ctrl and infected with SARS-CoV-2. For all experiments cells were infected with SARS-CoV-2 at an MOI of 0.1 and were treated with drugs 25-1000 nM for at least 2 hrs before infection and for 48 hpi. In all panels, data are representative or mean ± SEM of at least three experiments with at least 2 replicates. Statistical comparison was done between the Ctrl and each shown experimental group by using two-tailed Mann–Whitney (*$p < 0.05$, **$p < 0.01$, ***$p < 0.001$).

Figure S6 (related to Figure 3). Impact of Mito-MES on protein levels of Nrf2 in SARS-CoV-2 infected and uninfected epithelial cells. (**A** to **D**) Calu3 cells infected with SARS-CoV-2 (48 hrs) (MOI 0.1) and treated with Mito-MES (10-1000 nM, 72 hrs) and/or the Nrf2 agonist Dimethyl fumarate (DMF) (10, 100 μM, 16-24 hrs) and/or the Nrf2 inhibitor brusatol (0.25 μM, 16-24 hrs) or DMSO vehicle control (Ctrl). [(**A**), (**B**)] Protein levels (fluorescence intensity) of Nrf2 were determined by flow cytometry in total (infected and uninfected) (**A**) and SARS-CoV-2 infected (**B**) Calu3 cells. [(**C**), (**D**)] Viral replication (% of cells positive for the Nucleocapsid N SARS-CoV-2 protein) and Nrf2 protein levels (% of cells positive for the target protein) by flow cytometry at 48 hrs post infection in Calu3 cells treated with DMF and/or Mito-MES (**C**) or with brusatol and/or Mito-MES (**D**). Data in all panels are representative data from at least three independent experiments with at least 2 experimental replicates.

Figure S7 (related to Figure 3). Impact of Mito-MES on protein levels of Keap1 in SARS-CoV-2 infected and uninfected epithelial cells. (**A** to **D**) Calu3 cells infected with SARS-CoV-2 (48 hrs) (MOI 0.1) and treated with Mito-MES (10-1000 nM, 72 hrs) and/or the Nrf2 agonist Dimethyl fumarate (DMF) (10, 100 μM, 16-24 hrs) and/or the Nrf2 inhibitor brusatol (0.25 μM, 16-24 hrs) or DMSO vehicle control (Ctrl). (**A**) Viral replication (% of cells positive for the SARS-CoV-2 N protein) and Keap1 protein levels (% of cells positive for the target protein) by flow cytometry at 48 hrs post infection (hpi) in Calu3 cells treated with DMF and/or Mito-MES. (**B**) Keap1 fluorescence intensity was measured by flow cytometry in total (infected and uninfected) Calu3 cells treated with Mito-MES and/or DMF. (**C**) Viral replication and Keap1 protein levels by flow cytometry at 48 hpi in Calu3 cells treated with brusatol and/or Mito-MES. (**D**) Keap1 fluorescence intensity was measured by flow cytometry in total (infected and uninfected) Calu3 cells treated with Mito-MES and/or brusatol. Data in all panels are representative data from three or more independent experiments with at least 2 replicates.

Figure S8 (related to Figure 3). Impact of Mito-MES on protein levels of Heme oxygenase-1 (HO-1) in SARS-CoV-2 infected and uninfected epithelial cells. (**A** to **D**) Calu3 cells infected with SARS-CoV-2 (48 hrs) (MOI 0.1) and treated with Mito-MES (10-1000 nM, 72 hrs) and/or the Nrf2 agonist Dimethyl fumarate (DMF) (10, 100 μM, 16-24 hrs) and/or the Nrf2 inhibitor brusatol (0.25 μM, 16-24 hrs) or DMSO vehicle control (Ctrl). (**A**) Viral replication (% of cells positive for the Nucleocapsid N SARS-CoV-2 protein) and HO-1 protein levels (% of cells positive for the target protein) by flow cytometry at 48 hrs post infection (hpi) in Calu3 cells

treated with DMF and/or Mito-MES. (**B**) HO-1 protein level (fluorescence intensity) was quantified by flow cytometry in total (infected and uninfected) Calu3 cells treated with Mito-MES and/or DMF. (**C**) Viral replication and HO-1 protein levels by flow cytometry at 48 hpi in Calu3 cells treated with brusatol and/or Mito-MES. (**D**) HO-1 protein level (fluorescence intensity) was quantified by flow cytometry in total (infected and uninfected) Calu3 cells treated with Mito-MES and/or brusatol. Data panels are representative from three or more independent experiments with at least 2 replicates.

Figure S9 (related to Figure 3). Mitoquinone mesylate restricts SARS-CoV-2 associated apoptosis in epithelial cells. (A to **F)** Vero-E6 (**A** to **E**) and Calu3 (**F**) cells were treated with indicated doses of Mito-MES versus DMSO vehicle control (Ctrl) and infected with SARS-CoV-2 for 48 hrs (MOI of 0.1). (**A**) Panels show immunostaining for SARS-CoV-2 spike protein (red) and apoptosis marker cleaved caspase-3 (green) at 48 hrs post-infection (hpi) in cells treated with Ctrl or Mito-MES (250 nM). DAPI stained cell nuclei. Scale bar=100 μm. [(**B**), (**C**)] Summary of data for protein levels [% of cells positive for protein (**B**) and median fluorescence intensity (MFI)(**C**)] of cleaved caspase-3 in Vero-E6 were assessed by immunofluorescence. [(**D**), (**E**)] Protein levels [% of positive cells (**D**) and MFI (**E**)] of cleaved caspase-3 in Vero-E6 were assessed by flow cytometry. (**F**) Protein levels (% of positive cells) of cleaved caspase-3 in Vero-E6 were assessed by flow cytometry. In all panels, data are shown as summary data (mean ± SEM) or representative images of three or more independent experiments with at least 2 replicates. Unless otherwise stated, statistical comparison was done between the Ctrl and each shown experimental group by using two-tailed Mann–Whitney (*$p < 0.05$, **$p < 0.01$, ***$p < 0.001$).

Figure S10 (related to Figure 4). Gating strategy for flow panel A (assessment of SARS-CoV-2 Nucleocapsid protein among lung cell types). Representative data of gates: 1) Single cells based on forward scatter (FSC); → 2) Single cells based on side scatter (SSC). Cells were gated on the (1) gate; → 3) Viable non-red blood cells (non-RBCs) were gated as negative stain for the Violet Ghost dye (viability dye) and the BV421-Ter119 (mouse RBC marker). Cells were gated on the (2) gate; → 4) Cells (FSC/SSC) were gated to exclude debris; → 5) Non-immune lung cells were gated as CD45(-) on gate 4→ 6) Endothelial cells were gated as CD31(+) CD45(-

) cells on gate 5. 7) Lung epithelial cells were gated as CD326 [(epithelial cell adhesion molecule (EpCAM)] positive cells that were negative for CD31 and CD45 on gate 6; → 8) Alveolar type 2 (AT2) lung cells were gated as cells positive for the AT2 marker major histocompatibility complex class II (MHCII)) on lung epithelial cells in gate 7. 9) Alveolar type 1 (AT1) lung cells positive for the AT1 marker podoplanin but negative for MHCII on gate 8. 10) Ciliated lung cells positive for FOXJ1 but negative for podoplanin on gate 9.

Figure S11 (related to Figure 4). Mitoquinone mesylate inhibits SARS-CoV-2 replication in lung cells in mouse model of SARS-CoV-2 infection. hACE2 K18 mice (n=15) were infected with SARS-CoV-2 and treated intraperitoneally with Mito-MES (n=10) or vehicle control (Ctrl) (n=5) as in Fig. 4. Lung tissue was harvested on day 3 post infection. (**A** to **D**) Assessment of SARS-CoV-2 N protein by flow cytometry in EPCAM (+) lung epithelial cells [(**A**), (**B**)] and FOXJ1(+) EPCAM (+) ciliated cells [(**C**), (**D**)]. (**A**) Representative data for MFI of SARS-CoV-2 N protein in EPCAM (+) lung cells. (**B**) Summary data for (**A**). (**C**) Representative data for MFI of SARS-CoV-2 N protein in FOXJ1(+) EPCAM (+) ciliated cells. (**D**) Summary data for (**C**). Summary (means ± SEM) or representative data of at least three experiments in duplicates and triplicates are shown. Each datapoint represent a single sample. Unless otherwise shown, statistical comparison was done between the Ctrl and each shown experimental group by using two-tailed Mann–Whitney (*$p < 0.05$, **$p < 0.01$).

Figure S12 (related to Figure 4). Anti-SARS-COV-2 activity of Mito-MES in distal airway lung cells in hACE2 K18 mice. Mice were infected with SARS-CoV-2 and treated with Mito-MES (n=10) or vehicle control (Ctrl) (n=5) as in Fig. 4. Assessment of SARS-CoV-2 Nucleocapsid (N) protein by flow cytometry on day 3 post infection in alveolar type 1 (AT1) cells (**A** to **D**) AT2 lung cells (**E** to **H**) and CD31(+) CD45(-) endothelial cells (ECs) (**I** to **L**). [(**A**), (**B**)] Representative and summary data for % of infected AT1 cells. [(**C**), (**D**)] Representative and summary data for MFI of SARS-CoV-2 NP in AT1 cells. [(**E**), (**F**)] Representative and summary data for % of infected AT2 cells. [(**G**), (**H**)] Representative and summary data for MFI of SARS-CoV-2 NP in AT2 cells. [(**I**), (**J**)] Representative and summary data for % of infected endothelial cells. [(**K**), (**L**)] Representative and summary data for MFI of SARS-CoV-2 NP in endothelial cells. Summary (mean ± SEM) or representative data of at least three experiments in duplicates and triplicates are shown. Each datapoint represents one sample. Unless otherwise shown, statistical comparison was done between the Ctrl and each shown experimental group by using two-tailed Mann–Whitney (*$p < 0.05$, **$p < 0.01$).

Figure S13 (related to Figure 6). Mitoquinone mesylate inhibits SARS-CoV-2 associated inflammation and lung cell apoptosis in mouse model of SARS-CoV-2 infection. hACE2 K18 mice were infected intranasally with SARS-CoV-2 wild type (WT) or Beta variant (10,000 PFU/mouse), treated with Mito-MES 4 mg/kg/day or vehicle control (Ctrl). The lung tissue was harvested on day 3 (cohort A) or day 5-7 (cohort B) post infection, as shown in Fig. 6. (**A** to **D**) Supernatants from lung homogenates of mice from cohort A [(**A**), (**B**)] and B [(**C**), (**D**)] were used for measurement of cytokines using Luminex immunoassay. (**E**) Flow cytometry was used to assess frequency of CD45+ immune cells in lung cell suspension from mice infected with

SARS-CoV-2 Beta variant. (**F**) Assessment of SARS-CoV-2 nucleocapsid (N) protein and cleaved caspase 3 in lung tissues of mice from cohort B treated as shown. The sections were stained with anti-SARS-CoV-2 N (green), anti-cleaved caspase 3 (red) antibodies and DAPI (blue). White arrows show the SARS-CoV-2 N and caspase 3. Scale bars, 100 μm. Representative (**F**) or summary (**A** to **E**) data (mean ± SEM) from experiments in triplicates. Each datapoint represents one biological sample. Unless otherwise stated, statistical comparison was done between the Ctrl and each shown experimental group by using two-tailed Mann–Whitney (*$p < 0.05$, **$p < 0.01$).

Figure S14 (related to Figure 6). Gating strategy for flow panel B (assessment of frequency of immune cell types among lung cells isolated from mice infected with SARS-CoV-2). Representative data of gates: 1, 2) Single cells based on forward (FSC) and side scatter (SSC) → 3) Viable non-red blood cells (non-RBCs) were gated as negative stain for Violet Ghost dye (viability dye) and the BV421-Ter119 (mouse RBC marker). Cells were gated on the (2) gate; → 4) Cells (FSC/SSC) were gated to exclude debris; → 5) Immune cells were gated as CD45(+) on gate 4→ 8) Natural killer (NK) cells were gated as CD335 (NKp46) (+) cells on gate 7 major histocompatibility complex class II (MHCII) (CD11b (+) CD45(+) cells. 9) Neutrophils were gated as Ly-6G/Ly-6C(Gr-1) (+) cells on negative gate 7 [MHCII (-) CD11b (+) CD45(+)]. 10) Myeloid dendritic cells (DC) were gated as CD11c (+) cells on positive gate 7, 12) Monocytes/macrophages were gated as Ly-6G/Ly-6C(Gr-1) (+) cells on gate 11 [CD335 (NKp46) (-) CD11c (-) MHCII (+) CD11b (+) CD45(+) cells]. 13) Lymphoid dendritic cells

(DC) were gated as CD11c (+) cells on negative gate 6. 14) T cells were gated as CD3(+) cells on negative gate 6. 15) B cells were gated as CD19(+) cells on negative gate 14.

Figure S15 (related to Figure 6). Anti-inflammatory activity of Mito-MES in distal airway lung cells in hACE2 K18 mice. In cohort A mice were infected with wild type (WT) SARS-CoV-2 and treated with either vehicle control (saline 10% DMSO; Ctrl) (n=5) or mitoquinone mesylate (Mito-MES) 4 mg/kg/day (n=10) intraperitoneally either 24 hrs before the infection (hbi) (n=5) or 8 hrs post infection (hpi) (n=5) until day 3 post infection. In cohort B mice were infected with SARS-CoV-2 Beta variant and treated with Ctrl (n=10) or Mito-MES 4 mg/kg/day (n=10) intraperitoneally 24 hbi (n=10) until 5-7 days post infection. Lung tissue was harvested on day 3 (cohort A) or day 5-7 (cohort B) post infection. Assessment of frequency of immune cell subtypes in murine lung tissue by flow cytometry. Representative and summary data from mice in cohorts A and B treated with Mito-MES or Ctrl are shown for neutrophils (**A** to **C**), macrophages (**D** to **F**), myeloid dendritic cells (DCs) (**G** to **I**), lymphoid DCs (**J** to **L**), natural killer (NK) cells (**M** to **O**), T cells (**P** to **R**) and B cells [(**S**), (**T**)]. Statistical comparison was done between the Ctrl and each shown experimental group by using two-tailed Mann–Whitney (**p<0.01).

Figure S16 (related to Figures 1-6). Overall hypothesis and impact of Mito-MES on SARS-CoV-2 replication and associated inflammation and tissue damage. Mito-MES has antiviral, antiapoptotic and anti-inflammatory effect in epithelial cells infected with SARS-CoV-2. Mito-MES has pleiotropic cellular effects that collectively inhibit SARS-CoV-2 replication: 1) blocks

SARS-CoV-2 viral entry through its hydrophobic dTPP moiety; 2) inhibits cytoplasmic viral replication through a) its hydrophobic dTPP moiety, b) upregulation of antiviral host pathways (Nrf2 pathway, MX1, TOM70), c) downregulation of mitochondrial reactive oxygen species (mito-ROS) that induce proviral host factors for replication of coronaviruses such as the coatomer coat protein complex(de Wilde et al., 2015), the mitochondrial permeability transition pore (mPTP)(Halestrap et al., 2004), MEK (Zhang et al., 2016), MNK1(Wang and Zhang, 1999) and MAPK signaling pathways (Emerling et al., 2005; Kulisz et al., 2002; Trempolec et al., 2017) that propagate viral protein synthesis and replication (Jamaluddin et al., 2009; Kefaloyianni et al., 2006; Mizutani et al., 2004). Mito-ROS also alter interferon host responses(Agod et al., 2017), induce aberrant endoplasmic reticulum (ER) stress, lipid peroxidation, alterations of membranes and proteins and activation of cytosolic phospholipases (Adibhatla and Hatcher, 2008; Moon et al., 2012; Sun et al., 2012); 3) blocks SARS-CoV-2-associated cellular apoptosis and subsequent release of SARS-CoV-2 virions to infect other cells. Mito-MES has also anti-inflammatory properties (reduces release of IL-1β, IL-6, TNF-α) that are mediated partially through the Nrf2 pathway and its dTPP moiety. Collectively, the antiviral, antiapoptotic and anti-inflammatory effects of Mito-MES in epithelial cells infected with SARS-CoV-2 reduce tissue damage and morbidity from COVID-19. Created with Biorender.com and Avogadro.cc.

STAR METHODS

RESOURCE AVAILABILITY

Lead Contact

Further information and requests for resources and reagents should be directed to and will be fulfilled by the Lead Contact, Theodoros Kelesidis (tkelesidis@mednet.ucla.edu).

Materials availability

This study did not generate new unique reagents.

Data and code availability:

All data are available in the main text or the supplementary materials.

EXPERIMENTAL MODEL AND SUBJECT DETAILS

Cell cultures

Calu3, Vero-E6, HEK293-ACE2, Murine 17Cl-1 cells were maintained at 37 °C and 5% CO_2 in DMEM or MEM supplemented with 10% (v/v) FBS, penicillin (100 units/ml), and streptomycin (100 µg/ml) (1X P/S). HEK293-ACE2 cells were maintained at 37 °C and 5% CO_2 in MEM supplemented with 10% (v/v) FBS and hygromycin. Primary mouse lung cells that express

human ACE2 were isolated from uninfected K18-hACE2 mice and were maintained at 37 °C and 5% CO_2 in DMEM supplemented with 10% (v/v) FBS and 1X P/S.

Human Tissue Procurement

Large airways and bronchial tissues were acquired from de-identified normal human donors after lung transplantations at the Ronald Reagan University of California, Los Angeles (UCLA) Medical Center. Tissues were procured under Institutional Review Board-approved protocols at the David Geffen School of Medicine at UCLA. Human airway basal stem cells (ABSCs) from one biological replicate were used for two experiments. The biological replicates were from ABSCs isolated from lung transplant donors. No demographic data was available for the normal lung donor samples.

ABSC Isolation

Human airway basal stem cells (ABSCs) were isolated following a previously published method by our group(Purkayastha et al., 2020). Briefly, airways were dissected, cleaned, and incubated in 16 units/ml dispase for 30 minutes (min) at room temperature. Tissues were then incubated in 0.5 mg/ml DNase for another 30 min at room temperature. Epithelium was stripped and incubated in 0.1% (v/v) Trypsin- EDTA for 30 min shaking at 37 °C to generate a single cell suspension. Isolated cells were passed through a 40 μm strainer and plated for Air-Liquid Interface cultures.

ABSC Air-Liquid Interface Cultures (Upper airway ALI cultures)

24-well 6.5 mm transwells with 0.4 μm pore polyester membrane inserts were coated with collagen type I dissolved in cell culture grade water at a ratio of 1:10. 100 μl was added to each transwell and allowed to air dry. ABSCs were seeded at 100,000 cells per well directly onto collagen-coated transwells and allowed to grow in the submerged phase of culture for 4-5 days with 500 μl media in the basal chamber and 200 μl media in the apical chamber. ALI cultures were then established and cultured with only 500 μl media in the basal chamber, and cultures were infected with SARS-COV-2 as indicated. Media was changed every other day and cultures were maintained at 37 °C and 5% CO_2.

Human Primary Small Airway Epithelial Cells (HSAECs) Lower Respiratory Epithelium Airway ALI cultures

HSAECs were seeded onto collagen coated transwells and grown in the submerged phase of culture for 4–5 days in PneumaCult Ex Plus media with 500 μl media in the basal chamber and 200 μl media in the apical chamber. ALI cultures were then maintained for 21 days with only 500 μl PneumaCult ALI media in the basal chamber, and media changed every 2 days. Cultures were maintained at 37 °C and 5% CO_2.

SARS-CoV-2 infection

All studies involving live virus were conducted at the UCLA Biosafety Level 3 (BSL3) high-containment facility with appropriate institutional biosafety approvals. SARS-CoV-2 was passaged once in Vero-E6 cells and viral stocks were aliquoted and stored at –80 °C. Virus titer was measured in Vero-E6 cells by median tissue culture infectious dose ($TCID_{50}$) assay. Cell

cultures in 96 well plates and ALI cultures were infected with SARS-CoV-2 viral inoculum [Multiplicity of infection (MOI) of 0.1 or at least 1 for ALI; 100 µl/well] prepared in media. For infection of Calu3 cells in 96 well plates with the fluorescent reporter a stable mNeonGreen SARS-CoV-2 virus (icSARS-CoV-2-mNG), an MOI of 0.3 and 100 µl/well was used. For mock infection, conditioned media (100 µl/well) alone was added.

Assessment of SARS-CoV-2 infection among different cell culture systems

SARS-CoV-2 infection was assessed by independent experiments that determined either the single cell content of SARS-CoV-2 or the total amount of secreted, intracellular or total (secreted and intracellular) SARS-CoV-2. The intracellular content of the SARS-CoV-2 nucleocapsid protein (NP) or the Spike (S) protein was assessed using ELISA, flow cytometry and immunofluorescence as described in Methods. Protein extract concentration was quantified using the Pierce BCA Protein Assay, according to manufacturer instructions (Thermo Fisher Scientific, Waltham, MA). SARS-CoV-2 NP or S protein content was expressed as either the percentage of cells that were positive for the SARS-CoV-2 viral protein (immunofluorescence or flow cytometry) or the median fluorescence intensity (MFI) of the SARS-CoV-2 viral protein per cell (immunofluorescence or flow cytometry). In ELISA experiments the intracellular SARS-CoV-2 NP or S protein content (pg) was normalized by the total cellular amount of protein within each experimental well (pg of viral protein per µg of total protein). The intracellular genomic expression of SARS-CoV-2 was assessed using primers specific for SARS-CoV-2 and real time PCR as described in Methods. The secreted amount of SARS-CoV-2 in cell culture supernatant of infected cell cultures was assessed using SARS-CoV-2 NP ELISA. The secreted amount of live SARS-CoV-2 in cell culture supernatant of infected cell cultures was assessed using viral

titer as described in Methods. Percent infection was quantified as ((Infected cells/Total cells) - Background) *100 and the vehicle control was then set to 100% infection for analysis. The half maximal inhibitory concentration (IC_{50}) for each experiment were determined using the Prism (GraphPad Holdings, San Diego, CA) software.

Viral titers

Infectious titers were quantified by limiting dilution titration using Vero-E6 cells. Briefly, Vero-E6 cells were seeded in 96-well plates at 5,000 or 10,000 cells/well. The next day, SARS-CoV-2-containing supernatant was applied at serial 10-fold dilutions ranging from 10^{-1} to 10^{-8} and, after 3-5 days, viral cytopathic effect (CPE) was assessed by microscopy or by determination of the intracellular SARS-CoV-2 NP using ELISA. $TCID_{50}$/ml was calculated using the Reed-Muench method.

In-cell SARS-CoV-2 ELISA

To independently establish detection of SARS-CoV-2 infection using a more quantitative method to assess viral titer (not based on microscopy), we utilized in-cell SARS-CoV-2 ELISA based on intracellular detection of the SARS-CoV-2 S or NP protein. 5,000 or 10,000 Vero-E6 cells were seeded in 96 well plates in 100 µl. The next day, the cells were inoculated with 10 µl of a 10-fold titration series of SARS-CoV-2. Two to three days later, SARS-CoV-2 S or NP protein staining was assessed using an anti-SARS-CoV-2 S or NP protein antibody. Cells were fixed by adding 100 µl 8% (v/v) PFA to 100 µl of medium (final 4% solution) and 30 min of room temperature incubation. Medium was then discarded and the cells permeabilized for 5 min at room temperature by adding 100 µl of Intracellular Staining Permeabilization Wash Buffer

(BioLegend). Cells were then washed with PBS and stained with 1:5,000 (anti-Spike S antibody clone 1A9) or 1:10,000 (anti-NP antibody clone ARC2372) in permeabilization buffer at 37 °C. After 1 hour, the cells were washed three times with washing buffer before a secondary anti-mouse or anti-rabbit antibody conjugated with HRP was added (1:20,000) and incubated for 1 hour at 37 °C. Following three times of washing, the 3,3′,5,5′-tetramethylbenzidine (TMB) peroxidase substrate was added. After 5 min light-protected incubation at room temperature, reaction was stopped using 0.5 M H2SO4. The optical density (OD) was recorded at 450 nm and baseline corrected for 620 nm using the Biotek microplate reader (Agilent Technologies, Santa Clara, CA).

Drug treatments

A concentration of Mito-MES between 10-1000 nM has been shown to be physiologically relevant, efficacious and non-cytotoxic in human mammalian cells. The antiviral activity of Mito-MES was evaluated in Calu3, Vero-E6, HEK293T and HSAECs ALI cell cultures. All SARS-CoV-2 studies were performed in biological triplicate. Cultured cells were incubated separately with Mito-MES or decyl triphenyl phosphonium cation (DTPP) (0, 10, 100, 250, 500 or 1000 nM) — a non-antioxidant mitochondria-targeted control compound which allowed for the effects of the TPP component of Mito-MES to be examined. The concentration of DMSO vehicle control was maintained constant at 0.01% v/v for all treatments. Drug effects were measured relative to vehicle controls *in vitro*. Unless stated, as proof-of concept experiments and to ensure that adequate time was allowed for Mito-MES to alter host cellular responses in mitochondria enriched epithelial cells, Calu3, Vero-E6, HEK293-ACE2, and ALI cultures were pretreated for 16-24 hours (hrs) with the indicated treatments (Mito-MES, DMF, Brusatol, Mito-

TEMPO) or vehicle control. The cells were then washed, infected with SARS-CoV-2 for 2 hrs, the virus was removed, and the treatments (Mito-MES, mito-TEMPO, remdesivir) were added back. Remdesivir (5 μM), a well characterized direct acting antiviral agent was used as an antiviral control.

Assessment of cell cytotoxicity

To measure cell viability to determine if there was any treatment-induced cytotoxicity, uninfected cells were plated and treated with the same compound dilutions used for the *in vitro* efficacy studies. As above, 0.01% DMSO-treated cells served as the 0% cytotoxicity control. After 24-48 hrs, cell viability was measured on a Synergy 2 Biotek microplate reader (Agilent Technologies, Santa Clara, CA) via the XTT Cell Proliferation Assay Kit according to the manufacturer's protocol (ATCC, Manassas, VA). Similar data were obtained in three independent experiments. Flow cytometry was used to independently assess cell viability and levels of target proteins in single viable cells.

Imaging and immunofluorescence

After 24-48 hrs of SARS-CoV-2 infection (or mock), live cell images were obtained by wide field fluorescence microscopy using a 10x air objective (Leica DM IRB, Wetzlar, Germany). For immunofluorescence, separate wells of cells were fixed with 4% paraformaldehyde in phosphate-buffered saline (PBS) for 20 min. The fixed samples were then permeabilized and blocked for 1 hour in a "blocking solution" containing PBS with 2% bovine serum albumin, 5% donkey serum, 5% goat serum, and 0.3% Triton X-100. Primary antibodies were diluted in the blocking solution and added to samples overnight at 4 °C. The following antibodies and dilutions were used:

polyclonal rabbit anti-Tom70 (1:100), rabbit anti-SARS-CoV-2 Spike S1 (clone #007) (1:100), polyclonal rabbit anti-cleaved caspase-3 (1:200), polyclonal rabbit anti-SARS-CoV-2 NP (1:1000). Samples were then rinsed 5 times for 2 min each with PBS containing 0.3% (v/v) Triton X-100, followed by incubation with fluorescent-conjugated secondary antibodies diluted 1:1,000 in blocking buffer for 2 hrs at room temperature. Secondary antibodies were goat anti-rabbit Alexa Fluor 488 IgG, goat anti-mouse Alexa Fluor 546, goat anti-rabbit DyLight 650. Samples were then rinsed 5 times for 2 min each with PBS containing 0.3% Triton X-100, followed by DAPI diluted in PBS at 1:5000 for 10 min. Immunofluorescence (IF) images were obtained using an LSM880 Zeiss confocal microscope (Carl Zeiss GmbH, Jena, Germany) with Airyscan using a 20X air objective or a 63X Apochromat oil-immersion objective. Immunofluorescence images were quantified using CellProfiler 2.0(Kamentsky et al., 2011) (Broad Institute, Cambridge, MA). DAPI was used to count total cell numbers in order to obtain a percentage of cells positive for spike protein, cleaved caspase-3, or TOM70. Alternatively, 96-well plates were imaged using the Operetta (PerkinElmer, Waltham, MA) system.

<u>High-throughput imaging</u>

Cells plated in Greiner µClear 96-well plates were stained with antibodies for immunofluorescence as above and were imaged on Operetta high-content wide-field fluorescence imaging system using a 10X air objective. Fifteen fields were imaged per well with a similar field distribution across all wells. CellProfiler 2.0 was used to quantify cell counts and infection ratios(Kamentsky et al., 2011).

<u>Cellular reactive oxygen species analysis</u>

Vero-E6 or Calu3 cells were treated and infected with icSARS-CoV-2-mNG reporter virus as indicated for 24-48 hrs. Subsequently, cells were washed once with hanks buffered salt solution (HBSS) with calcium and magnesium, without phenol-red and stained for 10 min with 1 µg/ml Hoechst 33342 and 5 µM dihydroethidum (DHE) in HBSS. Following two washes with HBSS, cells were returned to an imaging medium without phenol red (low glucose DMEM, supplemented with 10% (v/v) FBS, 2 mM glutamine and 1 mM sodium pyruvate and 1X P/S and imaged with a Leica DM IRB wide field fluorescence microscope as described above using DAPI, GFP, and RFP filters. CellProfiler 2.0 was used to quantify cell counts, infection ratios per well, and DHE fluorescence intensity per cell(Kamentsky et al., 2011).

Flow cytometry

Within the UCLA BSL3 high-containment facility, SARS-CoV-2 infected and uninfected cells were resuspended in PBS and single cell suspensions were incubated with viability dye at 1:500 (Fixable Ghost Dye Red 780 or Ghost Dye Violet 450) for 20 min in the dark at room temperature. Cells were washed and appropriate antibodies were added to each tube and incubated in the dark for 20 min on ice. Cells were then washed and fixed with 4% (v/v) paraformaldehyde or methanol for 30 min at 4 °C. Cells were then washed and were transferred in polypropylene Eppendorf tubes (E-tubes) to BSL2 containment facility for further processing. Appropriate antibodies were added to each tube and incubated in the dark for 20 min on ice.

The following antibodies were used for staining in flow cytometry: PE/Cy7 anti-mouse CD3 (clone 17A2, 1:25), BV 605 anti-mouse CD8a (clone 53-6.7, 1:10), Alexa Fluor 647 anti-mouse/human CD11b (clone M1/70, 1:50), BV421 anti-mouse CD11c (clone N418, 1:10),

PerCP/Cy5.5 anti-mouse CD19 (clone 1D3/CD19, 1:10), PE/Cy7 anti-mouse CD31 (clone 390, 1:100), BV785 anti-mouse CD45 (clone 30-F11, 1:40), PE/Cy7 anti-human CD147 (clone HIM6, 1:10), BV421 anti-human CD304 (Neuropilin-1, clone 12C2, 1:20), BV605 anti-mouse CD326 (Ep-CAM, clone G8.8, 1:8)), PE anti-mouse CD335 (NKp46, clone 29A1.4, 1:10), BV711 MHC II anti-mouse I-A/I-E (clone M5/114.15.2, 1:25), APC/Cy7 anti-mouse Podoplanin (clone 8.1.1, 1:50), BV421 anti-mouse TER-119/Erythroid Cells (clone TER-119, 1:33), APC/Cy7 anti-mouse Ly-6G/Ly-6C (Gr-1, clone RB6-8C5, 1:25), rabbit anti-SARS-CoV-2 NP (clone ARC2372. 1:50), rabbit anti-SARS-CoV-2 Spike (clone 007, 1:50), mouse anti-SARS-CoV-2 Spike (clone 1A9, 1:50), anti-ACE-2 (polyclonal, 1:10), rabbit anti-human TMPRSS2 (polyclonal, 1:10), Alexa Fluor 647 anti-human Furin (clone 222722, 1:10), rabbit anti-human MAVS (clone D5A9E, 1:10), rabbit anti-human TOM70 (polyclonal,1:5), rabbit anti-human/mouse Alexa Fluor 647 cleaved caspase-3 (clone D3E9, 1:25), mouse anti-human, HO-1 (clone HO-1-2, 1:20), anti-MX1 (polyclonal, 1:10), Alexa Fluor 647 anti-human STING (clone 723505, 1:10). Rabbit anti-NRF2 (polyclonal, 1:50) anti-FOXJ1-CF647 (polyclonal, 1:10). Non-fluorescent unconjugated primary antibodies were conjugated with Mix-n-Stain CF488 or CF647 Antibody Labeling Kits from MilliporeSigma (Burlington, MA).

The cells were washed twice with PBS and were transferred to tubes for fluorescence activated cell sorting (FACS) analysis. Samples were acquired using an LSRFortessa™ flow cytometer and FACSDiva™ software (Becton Dickinson, Franklin Lakes, NJ). Data were analyzed using FlowJo™ software (Becton Dickinson, Franklin Lakes, NJ). At least 10,000 cells were acquired for each analysis and only live and singlet cells were chosen for analysis and gating (i.e., dead

cells and aggregates were excluded). Each representative flow plot was repeated at least 3 times. Single stain and also fluorescence minus one (FMO) controls were used in the presence of a given concentration of the antibody staining cocktail.

The flow cytometry experiments in single-cell suspensions obtained from enzymatically digested murine lungs were performed using similar methodology like the cell suspensions from cell cultures with the following specifications.

To determine SARS-CoV-2 NP expression at the single cell level among different cell subtypes in murine lung [lung EPCAM (+) epithelial cells, ciliated FOXJ-1(+) lung EPCAM epithelial cells, alveolar type 1 (AT1), alveolar type 2 (AT2), CD31(+) CD45(-) endothelial cells, CD45(+) immune cells], one aliquot of cells was stained with a mastermix of antibodies for surface (CD326, MHCII, CD45, CD31, podoplanin, red blood cell marker Ter119) and intracellular antigens (SARS-CoV-2 NP, FOXJ-1). Lung epithelial cells were gated based on the lung epithelial marker EPCAM (CD326) (Hasegawa et al., 2017). Ciliated lung epithelial cells were gated based on the intracellular marker f-box factor FOXJ-1(You et al., 2004). AT1 cells were gated based on the AT1 marker podoplanin(Nakano et al., 2018). To gate AT2 cells we utilized a previously validated methodology that established that the MHCII marker is an AT2 membrane marker, similarly to the pro-surfactant protein C (proSP-C)(Hasegawa et al., 2017). Murine immune lung cells were gated as mouse (m)-CD45(+) cells. Murine endothelial cells were gated as m-CD45(-)/m-CD31(+) cells. Lung epithelial cells were gated as m-CD45(-)/m-CD31(-)/m-EPCAM (+) cells. Lung ciliated epithelial cells were gated as m-CD45(-)/m-CD31(-)/m-EPCAM (+) FOXJ-1(+) cells. AT1 cells were gated as m-CD45(-)/m-CD31(-)/m-EPCAM (+)/m-

podoplanin (+) (AT1 marker)/ MHCII (-) (AT2 marker) cells. AT2 cells were gated as m-CD45(-)/m-CD31(-)/m-EPCAM (+)/m-podoplanin (-)/MHCII (+) (AT2 marker) cells.

To determine lung inflammation at the single cell level and cellular infiltration of murine lung with different immune cell subtypes [neutrophils, monocytes, macrophages, myeloid dendritic cells (mDCs), lymphoid dendritic cells (lymphoid DCs), natural killer cells (NK cells), T lymphocytes and B lymphocytes), one aliquot of lung cells was stained with a mastermix of antibodies for surface markers [CD11b, CD11c, CD8, CD3, CD19, CD45, NKp46, MHCII, Ly-6G/Ly-6C (Gr-1), red blood cell marker Ter119)]. To reliably gate immune cells, we utilized a previously validated methodology that established that the Ly6G/Ly6C markers are superior to Gr-1 for identifying murine neutrophils and that F4/80 is unreliable marker to identify certain immune cell subtypes (Rose et al., 2012). Murine immune lung cells were gated as mouse (m)-CD45(+) cells. T lymphocytes were gated as m-CD3(+)/m-CD45(+) cells. B lymphocytes were gated as m-CD3(-)/m-CD19(+)/ m-CD45(+) cells. NK cells were gated as m-CD11b(+)/m-MHCII(+)/m-NKp46(+)/m-CD45(+) cells. NKp46 is expressed by all natural killer (NK) cells but not by lymphocytes, granulocytes or myeloid cells(Westgaard et al., 2004). Non-activated neutrophils do not express MHCII(Hansch and Wagner, 2003) and are positive for Ly6G/Ly6C markers (Rose et al., 2012). Non-activated neutrophils were gated as m-CD11b (+)/m-MHCII (-)/m-Ly6G/Ly6C (+)/m-CD45(+) cells.

Lymphoid dendritic cells (labelled as lymphoid DCs) are positive for CD8 marker and negative for CD11b marker(Shortman and Liu, 2002). Lymphoid DCs were gated as m-MHCII(+)/m-CD8(+)/m-CD11c(+)/m-CD11b(-)/m-CD45(+) cells. Myeloid tissue dendritic cells (labelled as

myeloid DCs) are negative for CD8 marker and positive for CD11b marker(Shortman and Liu, 2002). Myeloid DCs were gated as m-MHCII(+)/m-CD8(-)/m-CD11c(+)/m-CD11b(+)/m-CD45(+) cells. Monocytes and monocyte derived macrophages (M/M) express CD11b (Misharin et al., 2013) and Ly-6G/Ly-6C(Gr-1)(Rose et al., 2012) but do not express NKp46 (Westgaard et al., 2004) and CD11c (Misharin et al., 2013). Monocytes/macrophages (M/M) were gated as m-Ly-6G/m-Ly-6C(m-Gr-1) (+)/(m-NKp46) (-)/m-CD11c(-)/m-MHCII(+)/m-CD11b(+)/m-CD45(+) cells.

Mitochondrial Reactive oxygen species analysis

After 24 hrs post infection, cells were collected and stained with 5 μM MitoSOX Red Mitochondrial reactive oxygen species (mito-ROS) indicator for 30 min at 37 °C. Cells were washed with PBS, fixed with 4% paraformaldehyde for 30 min at 4 °C and transferred to polypropylene FACS tubes. Cells were then analyzed using an LSR Fortessa flow cytometer and FACSDiva software), and data were analyzed using FlowJo software (Becton Dickinson, Franklin Lakes, NJ).

Biomarkers of inflammation

Protein levels of secreted IL-6 were determined in cell culture supernatants using ELISA kits according to the manufacturer (Bio-Techne, Minneapolis, MN). Luminex immunoassay was used to measure human cytokines [interleukin-1β (IL-1β), IL-8, IL-10, TNF-α, Vascular endothelial growth factor (VEGF)] secreted by Calu3 cells and airway lung epithelial cells in cell culture supernatants according to the manufacturer (Bio-Techne, Minneapolis, MN). A 4-Plex

ProcartaPlex assay (Thermo Fisher Scientific, Waltham, MA) was used to measure murine cytokines (IL-1β, IL-6, IL-18, TNF-α) in mouse lung protein lysates.

RNA extraction and Real-Time Quantitative Reverse Transcription Polymerase Chain Reaction (RT-qPCR)

Total RNA was isolated using the RNeasy Mini Kit or Direct-zol RNA Miniprep kit (Zymo Research) and complementary deoxyribonucleic acid (cDNA) was synthesized using oligo deoxythymine (dT) primers and RevertAid first strand cDNA synthesis kit. Quantitative real-time reverse transcription PCR was performed using SYBR Green Master Mix and primers specific for SARS-CoV-2 as well as glyceraldehyde 3-phosphate dehydrogenase (GAPDH) transcripts. The following primers were used: 2019-nCoV_N1-F: GACCCCAAAATCAGCGAAAT, 2019-nCoV_N1-R: TCTGGTTACTGCCAGTTGAATCTG; h-GAPDH-F: CCACCTTTGACGCTGGG; h-GAPDH-R: CATACCAGGAAATGAGCTTGACA. All qRT-PCR reactions were performed using BIO-RAD CFX96 Touch Real-Time PCR Detection System (Bio-Rad Laboratories, Hercules, CA) on 96-well plates. PCR reactions included SYBR Green RT-PCR Master Mix, 10 µM primers and 5 µl of cDNA. Reactions were incubated at 45 °C for 10 min for reverse transcription, 95 °C for 2 min, followed by 40 cycles of 95 °C for 15 seconds (sec) and 60 °C for 60 sec. Gene expression fold change was calculated with the Delta-delta-cycle threshold (DDCt) method. Viral RNA levels were normalized to GADPH as an endogenous control and depicted as fold change over mock infected samples.

Mitochondrial respirometry analysis

Calu3 cells were seeded at a density of 16,000 cells per well into 8-well Seahorse mini plates and allowed to attach for 24 hrs. Treatments were started 24 hrs before infection with SARS-CoV-2 (WA1 strain, MOI 0.1-0.5). Cells were infected for 48 hrs and subsequently analyzed by Seahorse respirometry. Briefly, growth media was replaced with Seahorse XF base media (supplemented with 2 mM glutamine and 1 mM sodium pyruvate, pH adjusted to 7.4) twice and respirometry assessed using a Seahorse XF HS Mini Analyzer (Agilent Santa Clara, CA) and the using the Mito Stress Test protocol. After basal respiration, mitochondrial proton leak was assessed after oligomycin injection, maximal respiration was assessed after Carbonylcyanide-4-(trifluoromethoxy)-phenylhydrazone (FCCP) injection, and non-mitochondrial respiration after rotenone, and antimycin A injection. Following the assay, cells were fixed in 4% (v/v) paraformaldehyde as described above and SARS-CoV-2 positive cells stained against SARS-CoV-2 nucleocapsid protein, and nuclei stained with DAPI. Wells were imaged using an LSM880 Zeiss confocal microscope (Carl Zeiss GmbH, Jena, Germany) with a 10X air objective and cell counts and infection ratios determined using CellProfiler 2.0. Agilent Wave 2.6 software (Agilent Santa Clara, CA) was used to normalize oxygen consumption rates to cell counts.

Mouse studies of SARS-CoV-2 infection

All the antiviral studies were performed in animal biosafety level 3 (BSL3) facility at University of California, Los Angeles. All work was conducted under protocols approved by the Institutional Animal Care and Use Committee (IACUC). We used a model of mice hemizygous for the expression of hACE2 gene (K18-ACE2) and we performed three studies in these mice to evaluate the *in vivo* efficacy of Mito-MES as antiviral and anti-inflammatory therapeutic agent in

SARS-CoV-2 infection. In total, we utilized 55 male and female 4 to12-week-old specific pathogen–free hemizygous for Tg(K18-ACE2)2Prlmn (Strain B6.Cg-Tg(K18-ACE2)2Prlmn/J, the Jackson laboratory strain 034860) mice. Animals were housed in individually ventilated cages, 5 mice per cage, on a 12-h light–dark cycle at 21–23 °C and 40–60% humidity. Mice were allowed free access to irradiated standard rodent diet (Tecklad 2914C) and sterilized water. Littermates of the same sex were randomly assigned to experimental groups and all animal studies included both male and female mice.

Cohort A included 15 male K18-hACE2 mice between 4 to 8 weeks of age (16-25 g). Mice were treated intraperitoneally with either vehicle control (normal saline 10% DMSO; Ctrl) (n=10) or Mito-MES 4 mg/kg/day (n=5) for at least 20 hrs before the infection (dose 1). Ten mice were then given a second dose of vehicle or Mito-MES and after 2 hrs were infected intranasally with wild type (WT) SARS-CoV-2 [10,000 plaque-forming unit (PFU)/mouse in <50 µl of PBS, day 0]. Mice were anesthetized with a mixture of ketamine/xylazine before each intranasal infection. Five mice were given intraperitoneally Mito-MES (first dose) 8 hrs post infection (hpi)(n=5). Additional doses of Mito-MES (n=10) or vehicle (n=5) were given on day 1 (24 hpi), day 2 (48 hpi) and day 3 (72 hpi). The body weight of mice was measured each day. Three days post infection (dpi) animals were humanely euthanized. Whole left lungs were harvested and were processed to create homogenates for viral titration via TCID50, single cell suspension for flow cytometry, or protein lysates for immunoassays. The total (secreted and intracellular) amount of SARS-CoV-2 NP in lung tissue homogenates (protein lysates) from mice infected with SARS-CoV-2 was assessed by SARS-CoV-2 NP ELISA. The total (secreted and intracellular) amount

of live SARS-CoV-2 in lung tissue homogenates from mice infected with SARS-CoV-2 was assessed by viral titer.

Cohort B included 20 female K18-hACE2 mice between 4 to 8 weeks of age (16-21 g). Mice were treated intraperitoneally with either vehicle control (normal saline 10% DMSO; Ctrl) (n=10) or Mito-MES 4 mg/kg/day (n=10) for at least 20 hrs before the infection (dose 1). Next day (Day 0), mice were then given a second dose of vehicle or Mito-MES and after 2 hrs were infected intranasally with Beta Variant of SARS-CoV-2 (10,000 PFU/mouse in <50 µl of PBS). Mice were anesthetized with a mixture of ketamine/xylazine before each intranasal infection. Additional doses of Mito-MES (n=10) or vehicle (n=10) were given on each day for up to 5-7 dpi. The body weight of mice was measured each day. 5-7 dpi animals were humanely euthanized. Whole left lungs were harvested and were processed for histopathology studies, single cell suspension for flow cytometry or protein lysates for immunoassays.

Cohort C included 20 male K18-hACE2 mice between 4 to 8 weeks of age (16-25 g). Mice were treated via gavage with either vehicle control (normal saline 10% DMSO; Ctrl) (n=10) or Mito-MES 20 mg/kg/day (n=10) for at least 20 hrs before the infection (dose 1). As source of Mito-MES the actual diet supplement capsule (5 mg Mito-MES per capsule) that is given in humans was utilized. Each capsule was opened and was dissolved in saline 10% DMSO solution before given via gavage to mice. Next day (Day 0), mice were then given a second dose of vehicle or Mito-MES and after 2 hrs were infected intranasally with Delta Variant of SARS-CoV-2 (10,000 PFU/mouse in <50 µl of PBS). Mice were anesthetized with a mixture of ketamine/xylazine before each intranasal infection. Additional doses of Mito-MES (n=10) or vehicle (n=10) were

given on day 1, day 2 and day 3 post infection. The body weight of mice was measured each day. On 3 dpi animals were humanely euthanized. Whole left lungs were harvested and were processed for single cell suspension for flow cytometry or viral titration via $TCID_{50}$.

Mouse tissue processing

Tissue samples were collected at necropsy. Less than 20 mg of lung tissue was either embedded in paraffin for hematoxylin and eosin (H&E) staining or was cryoembedded in Tissue-Plus O.C.T Compound for immunofluorescence staining. The right middle lobe was used for cell isolation and flow cytometry analysis. Tissues were weighted and <0.25 gram tissue samples were rinsed with DBPS, cut in 0.5 cm size pieces that were placed in 7 ml screwcap dissociation tubes with ceramic beads (Precellys) filled with 2.5 ml prewarmed (37 °C) digestion medium (2 mg/ml Collagenase, DNAse 0.1 mg/ml, 1% FCS). Tissues were mechanically dissociated at power 3,000 rpm for one 10-second cycle using a Precellys 24 homogenizer (Bertin Technologies, Montigny-le-Bretonneux, France), followed by a 30-minute incubation at 37 °C and another 10-second dissociation cycle (3,000 rpm). The homogenate was filtered through a sterile 40 μm nylon filter and cells were then processed for flow cytometry. The entire left lung was processed immediately for viral titer. Lung tissues were placed in 2 ml screwcap dissociation tubes with 60 X 1.4 mm ceramic beads at power 5,000 rpm using a Precellys 24 homogenizer and were mechanically dissociated in 0.5 ml DPBS for 90 sec. Homogenates were centrifuged at 16,000 g for 10 min and supernatants were then cryopreserved at –80 °C for viral titer in Vero-E6 cells. For tissue lysates that were used for protein measurements, 50-100 mg of lung tissue samples were placed in 2 ml screwcap dissociation tubes with ceramic beads (Precellys) and were mechanically dissociated in

T-PER tissue protein extraction Reagent at power 5,000 rpm leaving samples to cool on ice between 1–2 repeated 20-second cycles as previously described(Daskou et al., 2021).

Isolation of primary mouse lung cells

Following euthanasia, uninfected K18-hACE2 mice of identical age and gender like the mice in cohort C, were perfused with normal saline before removal of the left lung. Lung tissues were then rinsed with DBPS and processed similarly to SARS-CoV-2 infected mice to create cell suspension. Cells were then seeded in T75 flasks with complete medium [DMEM supplemented with 10% (v/v) FBS, 1X P/S] and were allowed to adhere overnight. The next day the medium was exchanged, and cells were maintained in complete medium before seeding in 96 well plates for SARS-CoV-2 infection and treatment with Mito-MES.

Mouse lung histological analysis

Paraffin-embedded murine lung tissue blocks were cut into 5 μm sections that were stained with hematoxylin and eosin (H&E) or Trichrome Masson. Light microscopic scans of whole lung were examined by an experienced pathologist using an Olympus BX53 microscope. Perivascular inflammation, airway inflammation, and alveolar inflammation were individually assessed semiquantitatively using a 5-point grading scheme considering the focality and intensity of the inflammatory infiltrate: 0 – absent, 1 – focal mild or patchy minimal, 2 – multifocal mild or focal moderate, 3 – diffuse moderate or focal severe, 4 – diffuse severe or with epithelial injury/necrosis. The overall grade of inflammation was determined using the sum of these three

scores (max 12). Interstitial and airway fibrosis were absent in all cases, confirmed by Masson trichrome stain.

QUANTIFICATION AND STATISTICAL ANALYSIS

Statistics

Unless noted, error bars in all figures represent mean and standard error of means (SEM). In the figures, p-values are presented for comparisons between treatment groups and controls and are denoted by asterisks. To pool cells from different experiments, each measurement was first normalized to the vehicle controls of each experiment. Each experiment contains at least 3 biological replicates (number of wells) and each analysis contains at least 2 independent experiments. For flow analysis of cells, at least 10,000 events were acquired for the population of interest. For analysis of data that contains more than 2 groups, the Kruskal-Wallis test was performed to compare samples; if these comparisons had a p value less than 0.05 then Mann-Whitney U tests were used to compare statistical difference between 2 groups. P-values less than 0.05 by Kruskal-Wallis or Mann-Whitney were considered significant. Consultation on statistical analysis was performed with the UCLA Biostatistics Department. All analyses were performed with GraphPad, version 8.0 (GraphPad Holdings, San Diego, CA).

References

Adibhatla, R.M., and Hatcher, J.F. (2008). Phospholipase A(2), reactive oxygen species, and lipid peroxidation in CNS pathologies. BMB Rep *41*, 560-567.

Agod, Z., Fekete, T., Budai, M.M., Varga, A., Szabo, A., Moon, H., Boldogh, I., Biro, T., Lanyi, A., Bacsi, A.*, et al.* (2017). Regulation of type I interferon responses by mitochondria-derived reactive oxygen species in plasmacytoid dendritic cells. Redox Biol *13*, 633-645.

Ansems, K., Grundeis, F., Dahms, K., Mikolajewska, A., Thieme, V., Piechotta, V., Metzendorf, M.I., Stegemann, M., Benstoem, C., and Fichtner, F. (2021). Remdesivir for the treatment of COVID-19. Cochrane Database Syst Rev *8*, CD014962.

Bizzotto, J., Sanchis, P., Abbate, M., Lage-Vickers, S., Lavignolle, R., Toro, A., Olszevicki, S., Sabater, A., Cascardo, F., Vazquez, E.*, et al.* (2020). SARS-CoV-2 Infection Boosts MX1 Antiviral Effector in COVID-19 Patients. iScience *23*, 101585.

Blair, H.A. (2019). Dimethyl Fumarate: A Review in Relapsing-Remitting MS. Drugs *79*, 1965-1976.

Braakhuis, A.J., Nagulan, R., and Somerville, V. (2018). The Effect of MitoQ on Aging-Related Biomarkers: A Systematic Review and Meta-Analysis. Oxid Med Cell Longev *2018*, 8575263.

Cao, H., Krueger, E.W., Chen, J., Drizyte-Miller, K., Schulz, M.E., and McNiven, M.A. (2020). The anti-viral dynamin family member MxB participates in mitochondrial integrity. Nat Commun *11*, 1048.

Codo, A.C., Davanzo, G.G., Monteiro, L.B., de Souza, G.F., Muraro, S.P., Virgilio-da-Silva, J.V., Prodonoff, J.S., Carregari, V.C., de Biagi Junior, C.A.O., Crunfli, F.*, et al.* (2020). Elevated

Glucose Levels Favor SARS-CoV-2 Infection and Monocyte Response through a HIF-1alpha/Glycolysis-Dependent Axis. Cell Metab *32*, 437-446 e435.

Daskou, M., Sharma, M., Mu, W., Heymans, R., Ritou, E., Rezek, V., Hamid, P., Kossyvakis, A., Sen Roy, S., Grijalva, V.*, et al.* (2021). ApoA-I mimetics favorably impact cyclooxygenase 2 and bioactive lipids that may contribute to cardiometabolic syndrome in chronic treated HIV. Metabolism *124*, 154888.

de Wilde, A.H., Wannee, K.F., Scholte, F.E., Goeman, J.J., Ten Dijke, P., Snijder, E.J., Kikkert, M., and van Hemert, M.J. (2015). A Kinome-Wide Small Interfering RNA Screen Identifies Proviral and Antiviral Host Factors in Severe Acute Respiratory Syndrome Coronavirus Replication, Including Double-Stranded RNA-Activated Protein Kinase and Early Secretory Pathway Proteins. J Virol *89*, 8318-8333.

Emerling, B.M., Platanias, L.C., Black, E., Nebreda, A.R., Davis, R.J., and Chandel, N.S. (2005). Mitochondrial reactive oxygen species activation of p38 mitogen-activated protein kinase is required for hypoxia signaling. Mol Cell Biol *25*, 4853-4862.

Fink, B.D., Herlein, J.A., Yorek, M.A., Fenner, A.M., Kerns, R.J., and Sivitz, W.I. (2012). Bioenergetic effects of mitochondrial-targeted coenzyme Q analogs in endothelial cells. J Pharmacol Exp Ther *342*, 709-719.

Halestrap, A.P., Clarke, S.J., and Javadov, S.A. (2004). Mitochondrial permeability transition pore opening during myocardial reperfusion--a target for cardioprotection. Cardiovasc Res *61*, 372-385.

Hansch, G.M., and Wagner, C. (2003). Expression of MHC class II antigen and coreceptor molecules in polymorphonuclear neutrophils. Chem Immunol Allergy *83*, 45-63.

Hasegawa, K., Sato, A., Tanimura, K., Uemasu, K., Hamakawa, Y., Fuseya, Y., Sato, S., Muro, S., and Hirai, T. (2017). Fraction of MHCII and EpCAM expression characterizes distal lung epithelial cells for alveolar type 2 cell isolation. Respir Res *18*, 150.

Hu, B., Guo, H., Zhou, P., and Shi, Z.L. (2021). Characteristics of SARS-CoV-2 and COVID-19. Nat Rev Microbiol *19*, 141-154.

Hu, M., Schulze, K.E., Ghildyal, R., Henstridge, D.C., Kolanowski, J.L., New, E.J., Hong, Y., Hsu, A.C., Hansbro, P.M., Wark, P.A*., et al.* (2019). Respiratory syncytial virus co-opts host mitochondrial function to favour infectious virus production. Elife *8*.

Jamaluddin, M., Tian, B., Boldogh, I., Garofalo, R.P., and Brasier, A.R. (2009). Respiratory syncytial virus infection induces a reactive oxygen species-MSK1-phospho-Ser-276 RelA pathway required for cytokine expression. J Virol *83*, 10605-10615.

James, A.M., Sharpley, M.S., Manas, A.R., Frerman, F.E., Hirst, J., Smith, R.A., and Murphy, M.P. (2007). Interaction of the mitochondria-targeted antioxidant MitoQ with phospholipid bilayers and ubiquinone oxidoreductases. J Biol Chem *282*, 14708-14718.

Kamentsky, L., Jones, T.R., Fraser, A., Bray, M.A., Logan, D.J., Madden, K.L., Ljosa, V., Rueden, C., Eliceiri, K.W., and Carpenter, A.E. (2011). Improved structure, function and compatibility for CellProfiler: modular high-throughput image analysis software. Bioinformatics *27*, 1179-1180.

Kefaloyianni, E., Gaitanaki, C., and Beis, I. (2006). ERK1/2 and p38-MAPK signalling pathways, through MSK1, are involved in NF-kappaB transactivation during oxidative stress in skeletal myoblasts. Cell Signal *18*, 2238-2251.

Kulisz, A., Chen, N., Chandel, N.S., Shao, Z., and Schumacker, P.T. (2002). Mitochondrial ROS initiate phosphorylation of p38 MAP kinase during hypoxia in cardiomyocytes. Am J Physiol Lung Cell Mol Physiol *282*, L1324-1329.

Lee, W.S., Wheatley, A.K., Kent, S.J., and DeKosky, B.J. (2020). Antibody-dependent enhancement and SARS-CoV-2 vaccines and therapies. Nat Microbiol *5*, 1185-1191.

Liu, X.Y., Wei, B., Shi, H.X., Shan, Y.F., and Wang, C. (2010). Tom70 mediates activation of interferon regulatory factor 3 on mitochondria. Cell Res *20*, 994-1011.

Misharin, A.V., Morales-Nebreda, L., Mutlu, G.M., Budinger, G.R., and Perlman, H. (2013). Flow cytometric analysis of macrophages and dendritic cell subsets in the mouse lung. Am J Respir Cell Mol Biol *49*, 503-510.

Mizutani, T., Fukushi, S., Saijo, M., Kurane, I., and Morikawa, S. (2004). Phosphorylation of p38 MAPK and its downstream targets in SARS coronavirus-infected cells. Biochem Biophys Res Commun *319*, 1228-1234.

Moon, S.H., Jenkins, C.M., Liu, X., Guan, S., Mancuso, D.J., and Gross, R.W. (2012). Activation of mitochondrial calcium-independent phospholipase A2gamma (iPLA2gamma) by divalent cations mediating arachidonate release and production of downstream eicosanoids. J Biol Chem *287*, 14880-14895.

Nakano, H., Nakano, K., and Cook, D.N. (2018). Isolation and Purification of Epithelial and Endothelial Cells from Mouse Lung. Methods Mol Biol *1799*, 59-69.

Nalbandian, A., Sehgal, K., Gupta, A., Madhavan, M.V., McGroder, C., Stevens, J.S., Cook, J.R., Nordvig, A.S., Shalev, D., Sehrawat, T.S.*, et al.* (2021). Post-acute COVID-19 syndrome. Nat Med *27*, 601-615.

Olagnier, D., Farahani, E., Thyrsted, J., Blay-Cadanet, J., Herengt, A., Idorn, M., Hait, A., Hernaez, B., Knudsen, A., Iversen, M.B., *et al.* (2020). SARS-CoV2-mediated suppression of NRF2-signaling reveals potent antiviral and anti-inflammatory activity of 4-octyl-itaconate and dimethyl fumarate. Nat Commun *11*, 4938.

Purkayastha, A., Sen, C., Garcia, G., Jr., Langerman, J., Shia, D.W., Meneses, L.K., Vijayaraj, P., Durra, A., Koloff, C.R., Freund, D.R., *et al.* (2020). Direct Exposure to SARS-CoV-2 and Cigarette Smoke Increases Infection Severity and Alters the Stem Cell-Derived Airway Repair Response. Cell Stem Cell *27*, 869-875 e864.

Rodriguez-Cuenca, S., Cocheme, H.M., Logan, A., Abakumova, I., Prime, T.A., Rose, C., Vidal-Puig, A., Smith, A.C., Rubinsztein, D.C., Fearnley, I.M., *et al.* (2010). Consequences of long-term oral administration of the mitochondria-targeted antioxidant MitoQ to wild-type mice. Free Radic Biol Med *48*, 161-172.

Rose, S., Misharin, A., and Perlman, H. (2012). A novel Ly6C/Ly6G-based strategy to analyze the mouse splenic myeloid compartment. Cytometry A *81*, 343-350.

Rossman, M.J., Santos-Parker, J.R., Steward, C.A.C., Bispham, N.Z., Cuevas, L.M., Rosenberg, H.L., Woodward, K.A., Chonchol, M., Gioscia-Ryan, R.A., Murphy, M.P., *et al.* (2018). Chronic Supplementation With a Mitochondrial Antioxidant (MitoQ) Improves Vascular Function in Healthy Older Adults. Hypertension *71*, 1056-1063.

Saha, S., Buttari, B., Panieri, E., Profumo, E., and Saso, L. (2020). An Overview of Nrf2 Signaling Pathway and Its Role in Inflammation. Molecules *25*.

Saidu, N.E., Noe, G., Cerles, O., Cabel, L., Kavian-Tessler, N., Chouzenoux, S., Bahuaud, M., Chereau, C., Nicco, C., Leroy, K., *et al.* (2017). Dimethyl Fumarate Controls the NRF2/DJ-1 Axis in Cancer Cells: Therapeutic Applications. Mol Cancer Ther *16*, 529-539.

1 Sena, L.A., and Chandel, N.S. (2012). Physiological roles of mitochondrial reactive oxygen
2 species. Mol Cell *48*, 158-167.
3 Shin, H.S., Kim, Y., Kim, G., Lee, J.Y., Jeong, I., Joh, J.S., Kim, H., Chang, E., Sim, S.Y., Park,
4 J.S.*, et al.* (2019). Immune Responses to Middle East Respiratory Syndrome Coronavirus During
5 the Acute and Convalescent Phases of Human Infection. Clin Infect Dis *68*, 984-992.
6 Shortman, K., and Liu, Y.J. (2002). Mouse and human dendritic cell subtypes. Nat Rev Immunol
7 *2*, 151-161.
8 Smith, R.A., and Murphy, M.P. (2010). Animal and human studies with the mitochondria-
9 targeted antioxidant MitoQ. Ann N Y Acad Sci *1201*, 96-103.
10 Sun, G.Y., He, Y., Chuang, D.Y., Lee, J.C., Gu, Z., Simonyi, A., and Sun, A.Y. (2012).
11 Integrating cytosolic phospholipase A(2) with oxidative/nitrosative signaling pathways in
12 neurons: a novel therapeutic strategy for AD. Mol Neurobiol *46*, 85-95.
13 Torres, J., Surya, W., Li, Y., and Liu, D.X. (2015). Protein-Protein Interactions of Viroporins in
14 Coronaviruses and Paramyxoviruses: New Targets for Antivirals? Viruses *7*, 2858-2883.
15 Trempolec, N., Munoz, J.P., Slobodnyuk, K., Marin, S., Cascante, M., Zorzano, A., and
16 Nebreda, A.R. (2017). Induction of oxidative metabolism by the p38alpha/MK2 pathway. Sci
17 Rep *7*, 11367.
18 Wang, Y., and Zhang, X. (1999). The nucleocapsid protein of coronavirus mouse hepatitis virus
19 interacts with the cellular heterogeneous nuclear ribonucleoprotein A1 in vitro and in vivo.
20 Virology *265*, 96-109.
21 Westgaard, I.H., Berg, S.F., Vaage, J.T., Wang, L.L., Yokoyama, W.M., Dissen, E., and Fossum,
22 S. (2004). Rat NKp46 activates natural killer cell cytotoxicity and is associated with
23 FcepsilonRIgamma and CD3zeta. J Leukoc Biol *76*, 1200-1206.

White, K.M., Rosales, R., Yildiz, S., Kehrer, T., Miorin, L., Moreno, E., Jangra, S., Uccellini, M.B., Rathnasinghe, R., Coughlan, L.*, et al.* (2021). Plitidepsin has potent preclinical efficacy against SARS-CoV-2 by targeting the host protein eEF1A. Science *371*, 926-931.

Winkler, E.S., Bailey, A.L., Kafai, N.M., Nair, S., McCune, B.T., Yu, J., Fox, J.M., Chen, R.E., Earnest, J.T., Keeler, S.P.*, et al.* (2020). SARS-CoV-2 infection of human ACE2-transgenic mice causes severe lung inflammation and impaired function. Nat Immunol *21*, 1327-1335.

You, Y., Huang, T., Richer, E.J., Schmidt, J.E., Zabner, J., Borok, Z., and Brody, S.L. (2004). Role of f-box factor foxj1 in differentiation of ciliated airway epithelial cells. Am J Physiol Lung Cell Mol Physiol *286*, L650-657.

Zhang, J., Wang, X., Vikash, V., Ye, Q., Wu, D., Liu, Y., and Dong, W. (2016). ROS and ROS-Mediated Cellular Signaling. Oxid Med Cell Longev *2016*, 4350965.

Zhang, S., Zhou, Q., Li, Y., Zhang, Y., and Wu, Y. (2020). MitoQ Modulates Lipopolysaccharide-Induced Intestinal Barrier Dysfunction via Regulating Nrf2 Signaling. Mediators Inflamm *2020*, 3276148.

Zhou, S., Hill, C.S., Sarkar, S., Tse, L.V., Woodburn, B.M.D., Schinazi, R.F., Sheahan, T.P., Baric, R.S., Heise, M.T., and Swanstrom, R. (2021). beta-d-N4-hydroxycytidine Inhibits SARS-CoV-2 Through Lethal Mutagenesis But Is Also Mutagenic To Mammalian Cells. J Infect Dis *224*, 415-419.

Zielonka, J., Joseph, J., Sikora, A., Hardy, M., Ouari, O., Vasquez-Vivar, J., Cheng, G., Lopez, M., and Kalyanaraman, B. (2017). Mitochondria-Targeted Triphenylphosphonium-Based Compounds: Syntheses, Mechanisms of Action, and Therapeutic and Diagnostic Applications. Chem Rev *117*, 10043-10120.

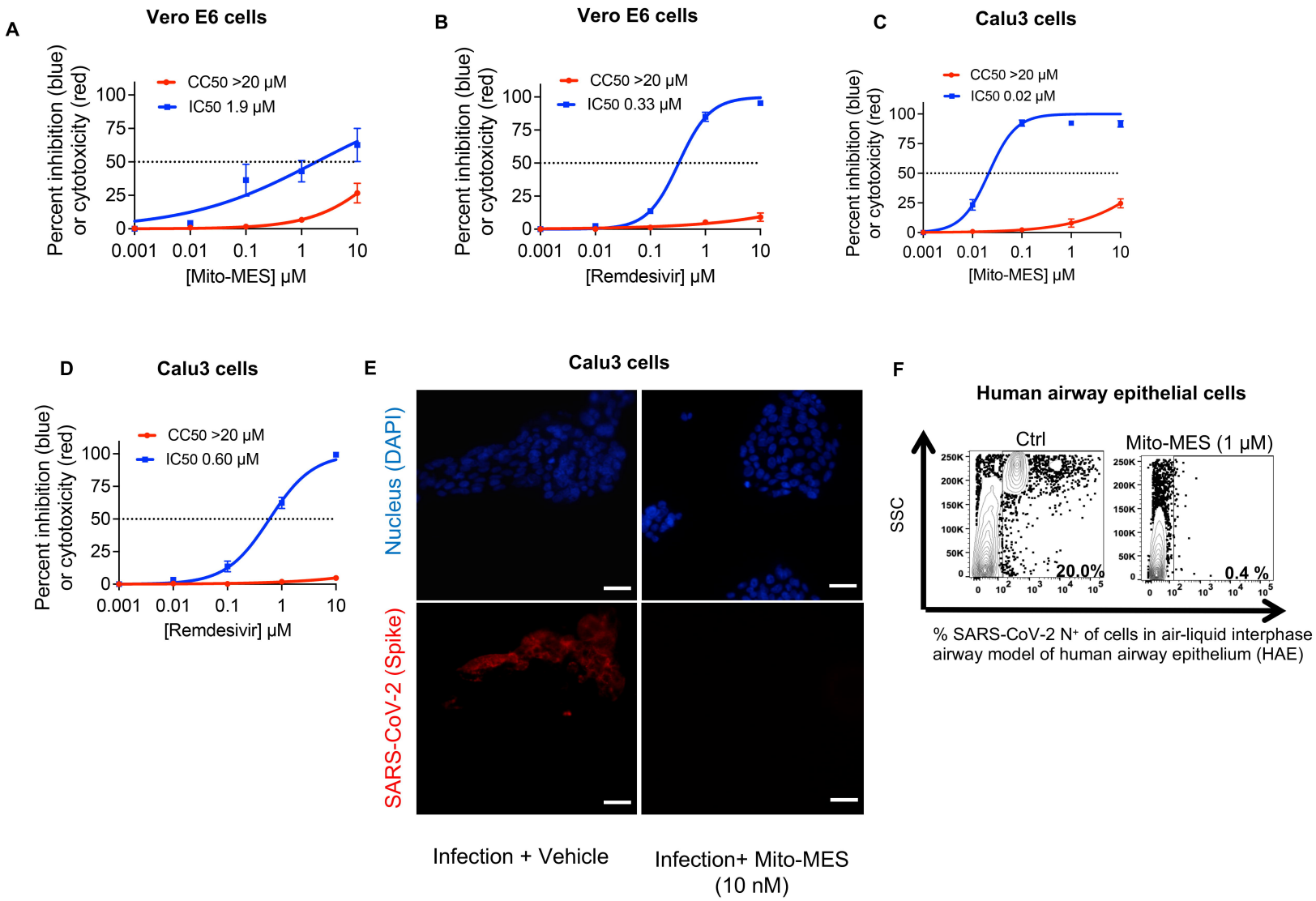
A
Vero E6 cells
Percent inhibition (blue) or cytotoxicity (red)
CC50 >20 μM
IC50 1.9 μM
[Mito-MES] μM
B
Vero E6 cells
CC50 >20 μM
IC50 0.33 μM
[Remdesivir] μM
C
Calu3 cells
CC50 >20 μM
IC50 0.02 μM
[Mito-MES] μM
D
Calu3 cells
CC50 >20 μM
IC50 0.60 μM
[Remdesivir] μM
E
Calu3 cells
Nucleus (DAPI)
SARS-CoV-2 (Spike)
Infection + Vehicle
Infection+ Mito-MES (10 nM)
F
Human airway epithelial cells
Ctrl
Mito-MES (1 μM)
SSC
20.0%
0.4 %
% SARS-CoV-2 N+ of cells in air-liquid interphase airway model of human airway epithelium (HAE)

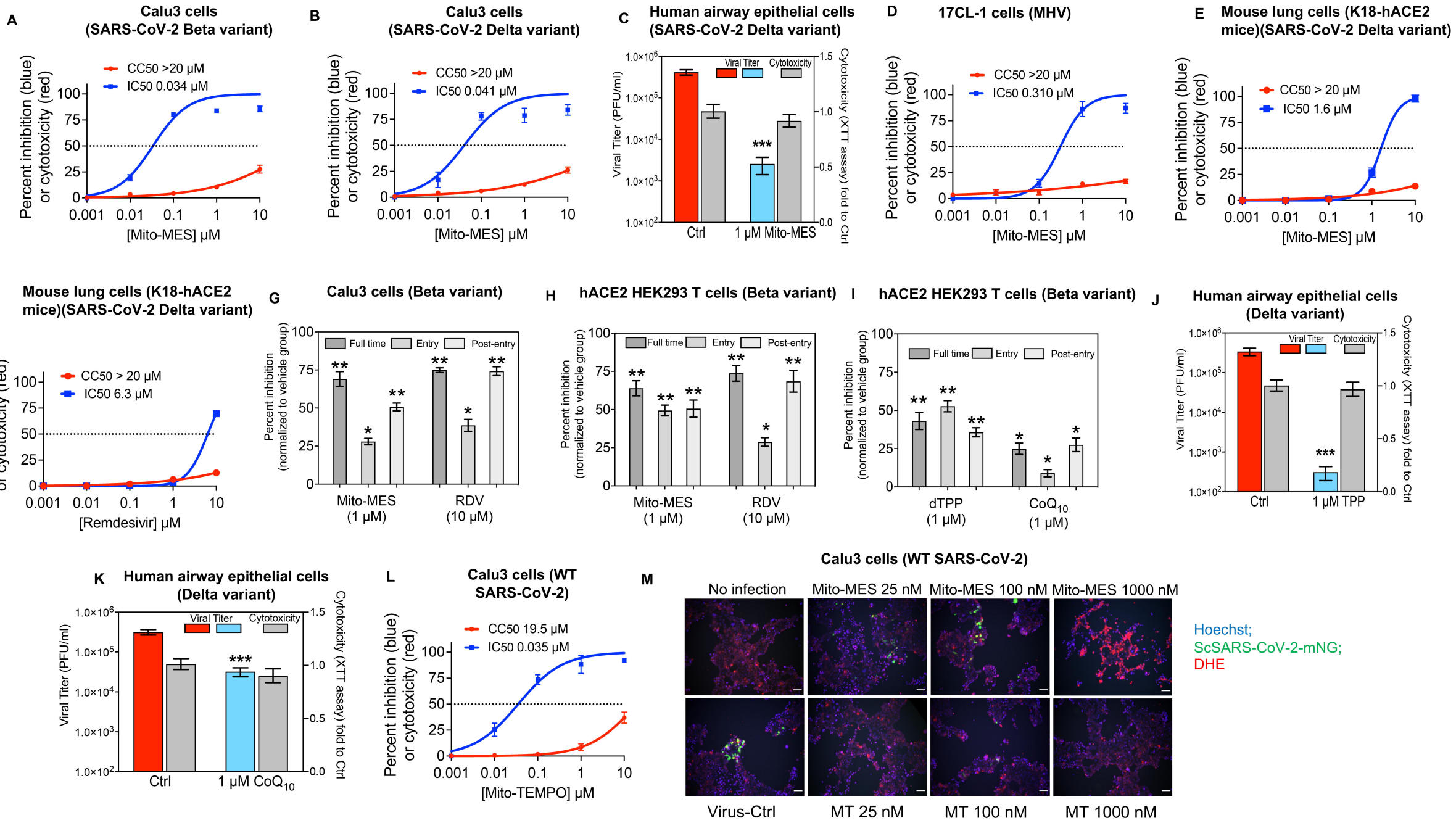
A
Calu3 cells
(SARS-CoV-2 Beta variant)
CC50 >20 μM
IC50 0.034 μM
Percent inhibition (blue)
or cytotoxicity (red)
[Mito-MES] μM
B
Calu3 cells
(SARS-CoV-2 Delta variant)
CC50 >20 μM
IC50 0.041 μM
[Mito-MES] μM
C
Human airway epithelial cells
(SARS-CoV-2 Delta variant)
Viral Titer
Cytotoxicity
Viral Titer (PFU/ml)
Cytotoxicity (XTT assay) fold to Ctrl
Ctrl
1 μM Mito-MES
D
17CL-1 cells (MHV)
CC50 >20 μM
IC50 0.310 μM
[Mito-MES] μM
E
Mouse lung cells (K18-hACE2
mice)(SARS-CoV-2 Delta variant)
CC50 > 20 μM
IC50 1.6 μM
[Mito-MES] μM
F
Mouse lung cells (K18-hACE2
mice)(SARS-CoV-2 Delta variant)
CC50 > 20 μM
IC50 6.3 μM
[Remdesivir] μM
G
Calu3 cells (Beta variant)
Full time
Entry
Post-entry
Percent inhibition
(normalized to vehicle group)
Mito-MES
(1 μM)
RDV
(10 μM)
H
hACE2 HEK293 T cells (Beta variant)
Full time
Entry
Post-entry
Percent inhibition
(normalized to vehicle group)
Mito-MES
(1 μM)
RDV
(10 μM)
I
hACE2 HEK293 T cells (Beta variant)
Full time
Entry
Post-entry
Percent inhibition
(normalized to vehicle group)
dTPP
(1 μM)
CoQ10
(1 μM)
J
Human airway epithelial cells
(Delta variant)
Viral Titer
Cytotoxicity
Viral Titer (PFU/ml)
Cytotoxicity (XTT assay) fold to Ctrl
Ctrl
1 μM TPP
K
Human airway epithelial cells
(Delta variant)
Viral Titer
Cytotoxicity
Viral Titer (PFU/ml)
Cytotoxicity (XTT assay) fold to Ctrl
Ctrl
1 μM CoQ10
L
Calu3 cells (WT
SARS-CoV-2)
CC50 19.5 μM
IC50 0.035 μM
Percent inhibition (blue)
or cytotoxicity (red)
[Mito-TEMPO] μM
M
Calu3 cells (WT SARS-CoV-2)
No infection
Mito-MES 25 nM
Mito-MES 100 nM
Mito-MES 1000 nM
Hoechst;
ScSARS-CoV-2-mNG;
DHE
Virus-Ctrl
MT 25 nM
MT 100 nM
MT 1000 nM

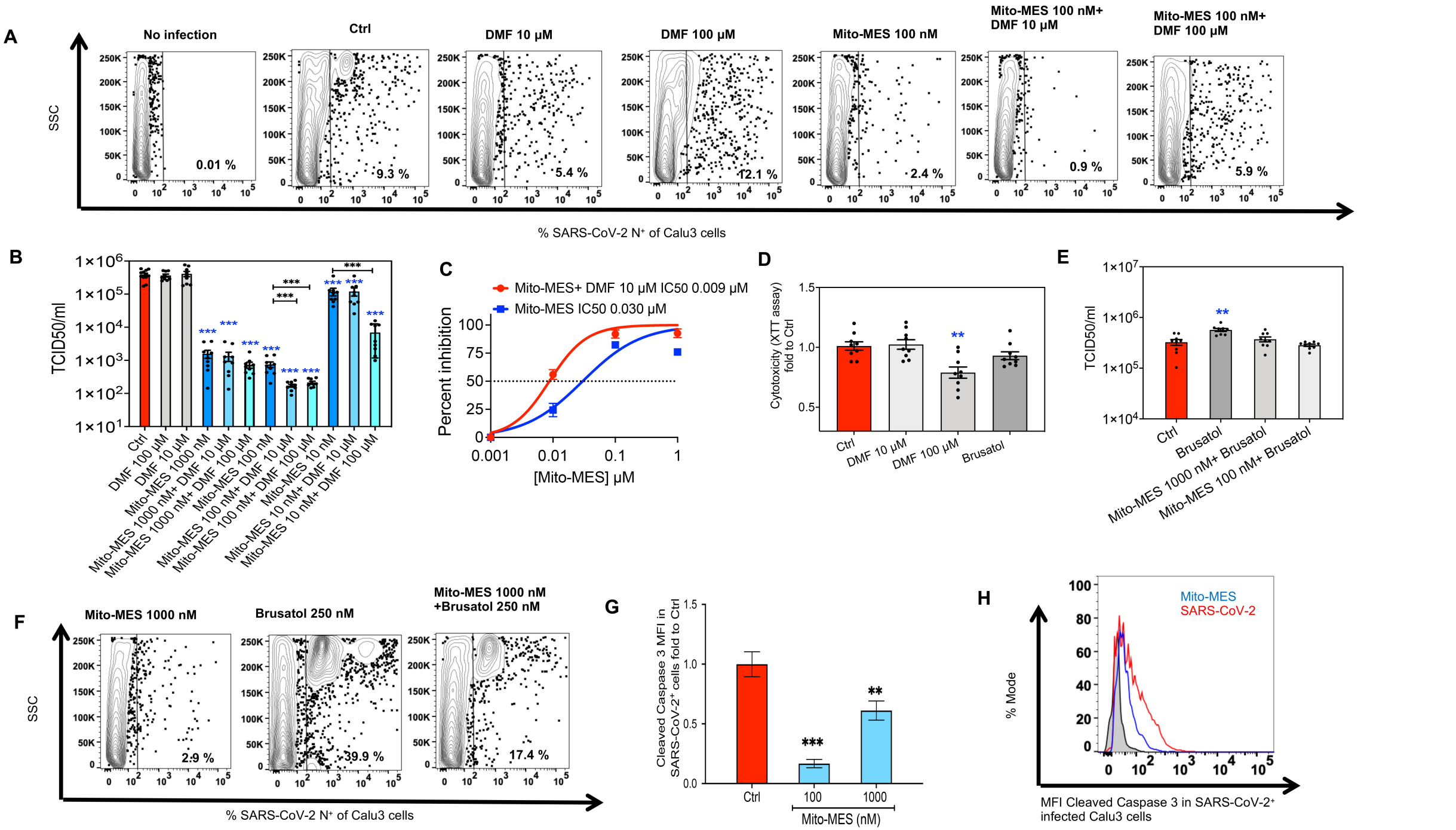
A
No infection
Ctrl
DMF 10 µM
DMF 100 µM
Mito-MES 100 nM
Mito-MES 100 nM+ DMF 10 µM
Mito-MES 100 nM+ DMF 100 µM
SSC
0.01 %
9.3 %
5.4 %
12.1 %
2.4 %
0.9 %
5.9 %
% SARS-CoV-2 N+ of Calu3 cells
B
TCID50/ml
Ctrl
DMF 100 µM
DMF 10 µM
Mito-MES 1000 nM
Mito-MES 1000 nM+ DMF 10 µM
Mito-MES 1000 nM+ DMF 100 µM
Mito-MES 100 nM
Mito-MES 100 nM+ DMF 10 µM
Mito-MES 100 nM+ DMF 100 µM
Mito-MES 10 nM
Mito-MES 10 nM+ DMF 10 µM
Mito-MES 10 nM+ DMF 100 µM
C
Mito-MES+ DMF 10 µM IC50 0.009 µM
Mito-MES IC50 0.030 µM
Percent inhibition
[Mito-MES] µM
D
Cytotoxicity (XTT assay) fold to Ctrl
Ctrl
DMF 10 µM
DMF 100 µM
Brusatol
E
TCID50/ml
Ctrl
Brusatol
Mito-MES 1000 nM+ Brusatol
Mito-MES 100 nM+ Brusatol
F
Mito-MES 1000 nM
Brusatol 250 nM
Mito-MES 1000 nM +Brusatol 250 nM
SSC
2.9 %
39.9 %
17.4 %
% SARS-CoV-2 N+ of Calu3 cells
G
Cleaved Caspase 3 MFI in SARS-CoV-2+ cells fold to Ctrl
Ctrl
100
1000
Mito-MES (nM)
H
% Mode
Mito-MES
SARS-CoV-2
MFI Cleaved Caspase 3 in SARS-CoV-2+ infected Calu3 cells

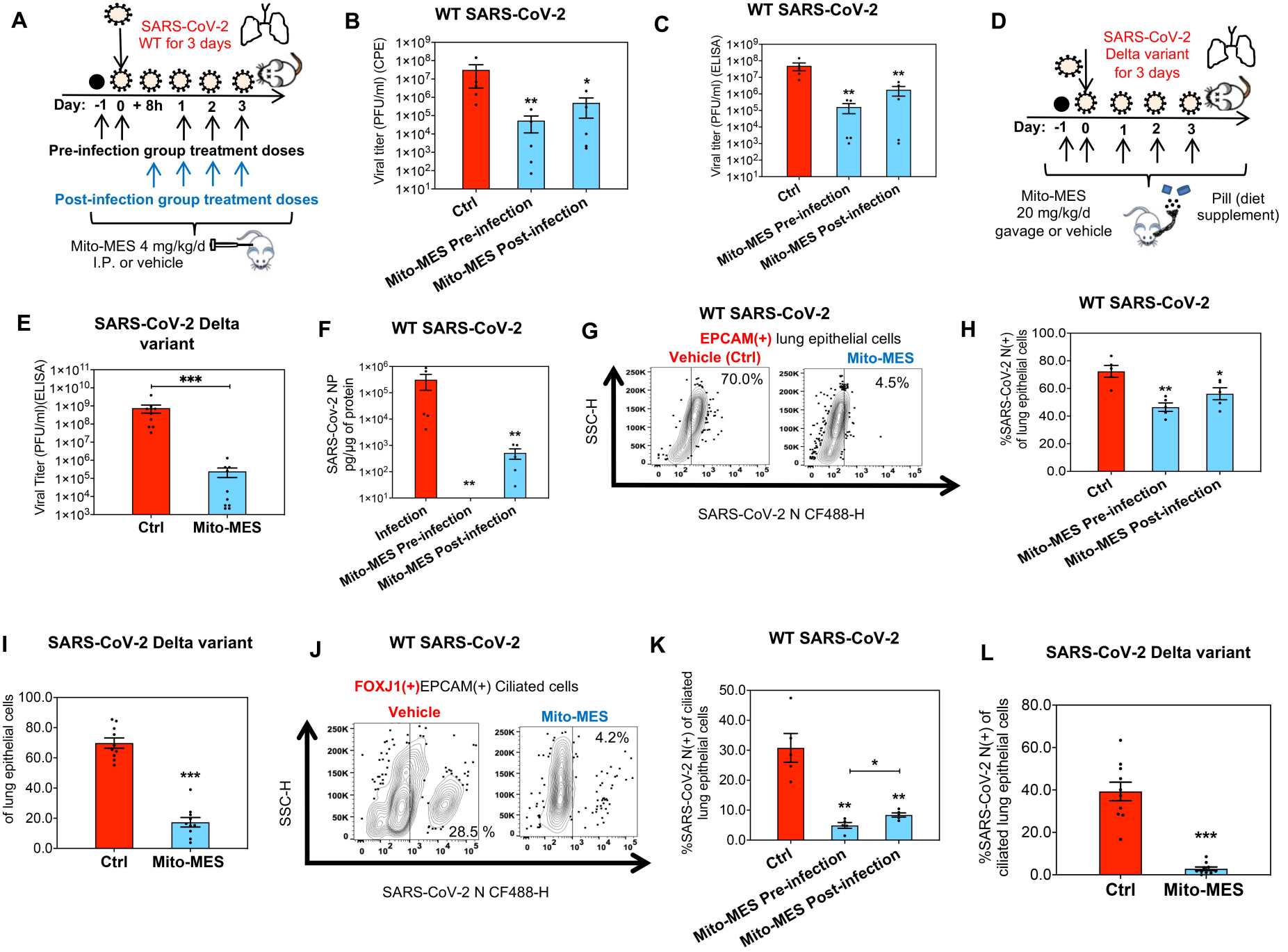
A
SARS-CoV-2
WT for 3 days
Day: -1 0 + 8h 1 2 3
Pre-infection group treatment doses
Post-infection group treatment doses
Mito-MES 4 mg/kg/d
I.P. or vehicle
B
WT SARS-CoV-2
Viral titer (PFU/ml) (CPE)
Ctrl
Mito-MES Pre-infection
Mito-MES Post-infection
C
WT SARS-CoV-2
Viral titer (PFU/ml) (ELISA)
Ctrl
Mito-MES Pre-infection
Mito-MES Post-infection
D
SARS-CoV-2
Delta variant
for 3 days
Day: -1 0 1 2 3
Mito-MES
20 mg/kg/d
gavage or vehicle
Pill (diet
supplement)
E
SARS-CoV-2 Delta
variant
Viral Titer (PFU/ml)(ELISA)
***
Ctrl
Mito-MES
F
WT SARS-CoV-2
SARS-Cov-2 NP
pg/μg of protein
Infection
Mito-MES Pre-infection
Mito-MES Post-infection
G
WT SARS-CoV-2
EPCAM(+) lung epithelial cells
Vehicle (Ctrl)
Mito-MES
70.0%
4.5%
SSC-H
SARS-CoV-2 N CF488-H
H
WT SARS-CoV-2
%SARS-CoV-2 N(+)
of lung epithelial cells
Ctrl
Mito-MES Pre-infection
Mito-MES Post-infection
I
SARS-CoV-2 Delta variant
%SARS-CoV-2 N(+)
of lung epithelial cells
***
Ctrl
Mito-MES
J
WT SARS-CoV-2
FOXJ1(+)EPCAM(+) Ciliated cells
Vehicle
Mito-MES
28.5 %
4.2%
SSC-H
SARS-CoV-2 N CF488-H
K
WT SARS-CoV-2
%SARS-CoV-2 N(+) of ciliated
lung epithelial cells
Ctrl
Mito-MES Pre-infection
Mito-MES Post-infection
L
SARS-CoV-2 Delta variant
%SARS-CoV-2 N(+) of
ciliated lung epithelial cells
***
Ctrl
Mito-MES

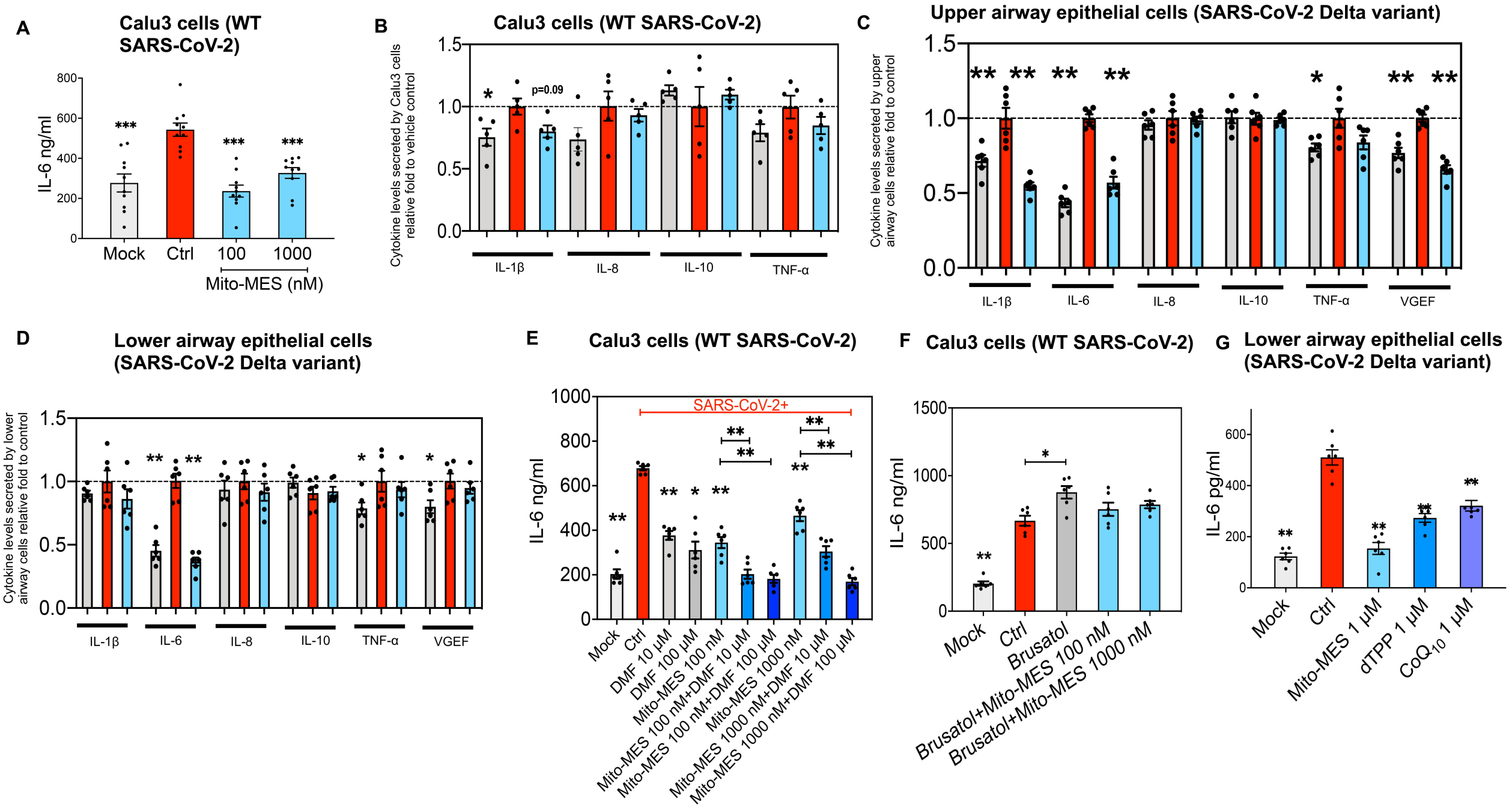
A
Calu3 cells (WT SARS-CoV-2)
IL-6 ng/ml
800
600
400
200
0
***
***
***
Mock
Ctrl
100
1000
Mito-MES (nM)
B
Calu3 cells (WT SARS-CoV-2)
Cytokine levels secreted by Calu3 cells relative fold to vehicle control
1.5
1.0
0.5
0.0
*
p=0.09
IL-1β
IL-8
IL-10
TNF-α
C
Upper airway epithelial cells (SARS-CoV-2 Delta variant)
Cytokine levels secreted by upper airway cells relative fold to control
1.5
1.0
0.5
0.0
** ** ** **
* ** **
IL-1β
IL-6
IL-8
IL-10
TNF-α
VGEF
D
Lower airway epithelial cells (SARS-CoV-2 Delta variant)
Cytokine levels secreted by lower airway cells relative fold to control
1.5
1.0
0.5
0.0
** **
* *
IL-1β
IL-6
IL-8
IL-10
TNF-α
VGEF
E
Calu3 cells (WT SARS-CoV-2)
IL-6 ng/ml
1000
800
600
400
200
0
SARS-CoV-2+
** ** ** ** ** ** ** ** ** **
Mock
Ctrl
DMF 10 μM
DMF 100 μM
Mito-MES 100 nM
Mito-MES 100 nM+DMF 10 μM
Mito-MES 100 nM+DMF 100 μM
Mito-MES 1000 nM
Mito-MES 1000 nM+DMF 10 μM
Mito-MES 1000 nM+DMF 100 μM
F
Calu3 cells (WT SARS-CoV-2)
IL-6 ng/ml
1500
1000
500
0
** * *
Mock
Ctrl
Brusatol
Brusatol+Mito-MES 100 nM
Brusatol+Mito-MES 1000 nM
G
Lower airway epithelial cells (SARS-CoV-2 Delta variant)
IL-6 pg/ml
600
400
200
0
** ** ** **
Mock
Ctrl
Mito-MES 1 μM
dTPP 1 μM
CoQ10 1 μM

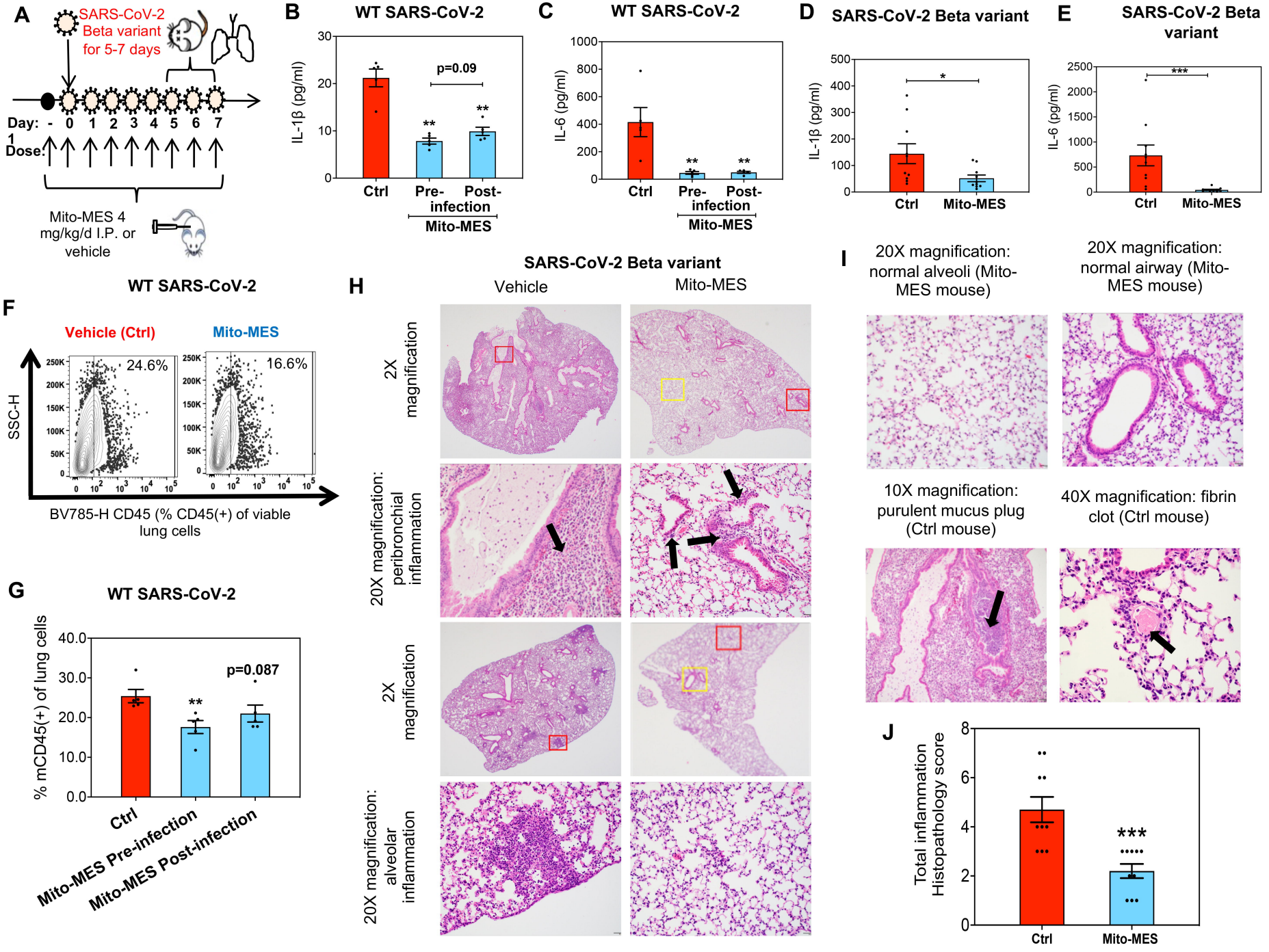
A
SARS-CoV-2 Beta variant for 5-7 days
Day: - 0 1 2 3 4 5 6 7
1 Dose:
Mito-MES 4 mg/kg/d I.P. or vehicle
B
WT SARS-CoV-2
IL-1β (pg/ml)
p=0.09
Ctrl
Pre-infection Mito-MES
Post-infection Mito-MES
C
WT SARS-CoV-2
IL-6 (pg/ml)
D
SARS-CoV-2 Beta variant
IL-1β (pg/ml)
Ctrl
Mito-MES
E
SARS-CoV-2 Beta variant
IL-6 (pg/ml)
F
WT SARS-CoV-2
Vehicle (Ctrl)
Mito-MES
24.6%
16.6%
SSC-H
BV785-H CD45 (% CD45(+) of viable lung cells
G
WT SARS-CoV-2
% mCD45(+) of lung cells
p=0.087
Ctrl
Mito-MES Pre-infection
Mito-MES Post-infection
H
SARS-CoV-2 Beta variant
Vehicle
Mito-MES
2X magnification
20X magnification: peribronchial inflammation
2X magnification
20X magnification: alveolar inflammation
I
20X magnification: normal alveoli (Mito-MES mouse)
20X magnification: normal airway (Mito-MES mouse)
10X magnification: purulent mucus plug (Ctrl mouse)
40X magnification: fibrin clot (Ctrl mouse)
J
Total inflammation Histopathology score
Ctrl
Mito-MES